Co-induced structural modulation in multiferroic Aurivillius-phase oxides

SCHOLARONE™
Manuscripts

Journal of Materials Chemistry C

Materials for optical, magnetic and electronic devices

ROYAL SOCIETY OF CHEMISTRY

Guidelines for Reviewers

Thank you very much for agreeing to review this manuscript for *Journal of Materials Chemistry C*.

Journal of Materials Chemistry C is a weekly journal in the materials field. The journal is interdisciplinary, publishing work of international significance on all aspects of materials chemistry related to applications in optical, magnetic and electronic devices. Articles cover the fabrication, properties and applications of materials.

Journal of Materials Chemistry C's Impact Factor is **6.641** (2018 Journal Citation Reports®)

The following manuscript has been submitted for consideration as a

FULL PAPER

For acceptance, a Full paper must report primary research that demonstrates significant **novelty and advance**, either in the chemistry used to produce materials or in the properties/ applications of the materials produced. Work submitted that is outside of these criteria will not usually be considered for publication. The materials should also be related to the theme of optical, magnetic and electronic devices.

When preparing your report, please:
- Focus on the **originality**, **importance**, **impact** and **reproducibility** of the science.
- Refer to the **journal scope and expectations**.
- **State clearly** whether you think the article should be accepted or rejected and give detailed comments (with references) both to help the Editor to make a decision on the paper and the authors to improve it.
- **Inform the Editor** if there is a conflict of interest, a significant part of the work you cannot review with confidence or if parts of the work have previously been published.
- **Provide your report rapidly** or inform the Editor if you are unable to do so.

Best regards,

Professor Peter Skabara
Editor-in-Chief
University of Glasgow, UK

Dr Sam Keltie
Executive Editor
Royal Society of Chemistry

Contact us

Please visit our reviewer hub for further details of our processes, policies and reviewer responsibilities as well as guidance on how to review, or click the links below.

What to do when you review

Reviewer responsibilities

Process & policies

Institute of
Materials Research
Slovak Academy of Sciences

Professor Federico Rosei
Associate Editor
Journal of Materials Chemistry C

May 11, 2020

Dear Professor Federico Rosei,

On behalf of all co-authors I would like to thank the referees for their valuable comments and suggestions to improve the manuscript. In the revised manuscript, we have addressed all the issues raised by the referees, and revised our manuscript accordingly. Since the original title ("Co-induced…") could have ambiguous meaning, we have slightly modified it to "Cobalt-induced structural modulation in multiferroic Aurivillius-phase oxides". Changes to the manuscript are highlighted in the text (in blue), and our specific responses to the referees' comments are given below.

Referee 1

In general, the manuscript has a correct methodological structure. But for my opinion the authors should making a major revision on this manuscript. I hope that authors reconsider these all points and they clarify some issues.

Comment 1. The authors should cited these references in Introduction section:

Journal of Magnetism and Magnetic Materials 430 (2017) 89–93; Journal of Magnetism and Magnetic Materials 405 (2016) 181–186; Journal of Alloys and Compounds 489 (2010) 441–444; Journal of Magnetism and Magnetic Materials 320 (2008) 1431–1435; Journal of Alloys and Compounds 503 (2010) 299–302; Physica B 407 (2012) 27–32; Journal of Magnetism and Magnetic Materials 322 (2010) 301–304; Journal of Physics and Chemistry of Solids 69 (2008) 2928–2931; Superlattices and Microstructures 84 (2015) 165–169; Journal of Magnetism and Magnetic Materials 398 (2016) 20–25; Journal of Alloys and Compounds 622 (2015) 761–764; Journal of Alloys and Compounds 581 (2013) 776–781; Journal of Magnetism and Magnetic Materials 378 (2015) 37–40.

We thank the reviewer for pointing out these studies. Although of good quality, the listed articles are devoted to spinel-type ferrites which is not the main focus of the present work; therefore it would be difficult and in some ways inappropriate to cite all the suggested studies in the introduction. In addition, although, the structural analysis of our samples suggested the presence of spinel-type impurities in the Aurivillius compounds, most of the references suggested are not focused on the actual Fe-rich and/or Co-rich secondary phases found in our samples, whose amount is by the way very low. However, some of the suggested studies could be useful to support the magnetic nature of the spinel phases found as possible minor impurities in our samples. So additional references on Fe-rich spinel phases such as have been added on page 22, as follows:

"Thus, these spinel-type impurities, although magnetic in nature [50,51], are unlikely to be the main contributors to the measured magnetization above room temperature."

[50] M. Ben Ali, K. El Maalam, H. El Moussaoui, O. Mounkachi, M. Hamedoun, R. Masrour, E. K. Hlil, A. Benyoussef, Effect of zinc concentration on the structural and magnetic properties of mixed Co–Zn ferrites nanoparticles synthesized by sol/gel method, *Journal of Magnetism and Magnetic Materials*, 2016, **398**, 20–25.

[51] M. Ben Ali, O. Mounkachi, K. El Maalam, H. El Moussaoui, M. Hamedoun, E. K. Hlil, D. Fruchart, R. Masrour, A. Benyoussef, Coexistence of blocked, metamagnetic and canted ferrimagntic phases at high temperature in Co–Nd ferrite nanorods, *Superlattices and Microstructures*, 2015, **84**, 165–169.

Comment 2. The author should give the motivation of ferroelectric Aurivillius-phase oxides in Introduction section.

In Introduction, the motivation of the present work and the choice of Aurivillius-phase oxides are presented distinctly in relevant sections (see below).

p.2 "Most of them are ferroelectric and the introduction of magnetic ions in perovskite-like layers can give rise to the occurrence of a long-range magnetic order. Owing to their good ferroelectric properties, such as Curie temperatures well above room temperature and low fatigue [5], Aurivillius-family compounds are considered as the most promising candidate for magnetoelectric-active multiferroic materials.[6-8]"

p.4 "To address the most compelling question on the origin of ferromagnetism in Co-substituted BFTO-derived compounds, we prepared polycrystalline samples in the $Bi_{4.3}Gd_{0.7}(Fe_{1-x}Co_x)_{1+y}Ti_{3-2y}Nb_yO_{15}$ (x=0, 0.3, 0.5 and y=0, 0.3) series and investigated the effect of the cobalt substitution on the crystal chemistry and macroscopic magnetization of these Aurivillius materials."

To emphasize the main goal even more, we added in Introduction (page 4) the following:

"Apparently, the method of the A-site rare-earth ion doping combined with the B-site 3*d*-transition metals co-substitution (e.g., the Fe/Co co-substitution) is an effective way to optimize ferromagnetic and ferroelectric properties of the bismuth-layered Aurivillius phases, and obtain a single phase multiferroic material displaying large magnetoelectric coefficient at room temperature. Our recent studies on the room-temperature multiferroic properties of the La-doped three- and four- layered BFCT compounds have proven the efficacy of this strategy, by yielding a single phase multiferroic material with the intrinsic magnetoelectric coupling at room temperature.[8,22]"

Comment 3. The authors should give the essential of their work in abstract and conclusions sections.

The authors believe that Abstract and Conclusions already describe the main results of the work. In order to address the referee's comment and present the essential of the work even more obvious, we added in Abstract (page 2) the following:

"The occurrence and enhancement of the magnetization in the ferroelectric Co-doped Aurivillius ceramics is attributed, respectively, to the NSM and the population of the ferromagnetic clusters nearby the interface of the four- and three- layered phases."

Comment 4. The authors should give the structure more stable (magnetic and crystalline structure) for their compounds.

The detailed structural (complementary techniques of synchrotron X-ray diffraction and thermogravimetry) and magnetic-property (ZFC-FC magnetization and AC susceptibility) analyses have evidenced well-crystallized stable structures with unique multiferroic properties at room temperature.

Comment 5. The ☐-Bi2O3☐☐☐Bi2O3 this transformation should be more explain.

To elaborate the formation of $Bi_{12}TiO_{20}$ in the Bi_2O_3-TiO_2 system, the section on the polymorphic transformation in Bi_2O_3 is modified in the revised manuscript (page 8), as follows:

The endothermic peaks at about 801K and 850 K are close to the melting point of the γ-Bi_2O_3-based surface phase ($T_m^{surf} \approx 823$-853 K [37]) at which the two solid-state reactions (α-$Bi_2O_3 \rightarrow Bi_{12}TiO_{20}$ and α-$Bi_2O_3 \rightarrow Bi_{24}Fe_2O_{39}$) are supposed to take place very fast. It has been reported that the α-$Bi_2O_3 \rightarrow Bi_{12}TiO_{20}$ transformation, which does not require changes in chemical bonds nor significant activation of the mass transfer (only 1 mol of TiO_2 should be incorporated per 12 mol of $BiO_{1.5}$ units), occurs readily, leading to the formation of the $Bi_{12}TiO_{20}$ sillenite at temperatures slightly below the melting points of the non-autonomous phases in the Bi_2O_3-TiO_2 system.[35]

Comment 6. In Fig.6, the superparamganetic behaviour is observed for all system and the ferromagnetic is not observed such as given in Fig.7. May be inverse the temperature value in Fig.6a and 6b.

The shape of the M-H loops in Fig.6 does not resemble a superparamagnetic behaviour, where an anhysteretic field dependence of magnetization is expected and coercivity should be absent. Therefore, hysteresis loops with a relatively small but finite coercivity observed in our case do not support the superparamagnetic nature of these systems (see also Fig. S3 in Supplementary material). The temperature value in Figs.6a and 6b is correct. On the other hand, the proposed spin glass-like behaviour of the samples under investigation is supported by the ZFC-FC curves (Fig. 10 and Fig. S6), and model calculations in Supplementary (see Fig. S8 and Fig. S9).

Comment 7. The authors should give the thermal polarization because they talk about the multiferoic

The thermal evolution of the ferroelectric polarization could have been revealed by the measurement of the pyroelectric current, but the relative equipment is not available in our labs. However, in the doped samples, multiferroicity at room temperature has been demonstrated by the existence of the ferroelectric polarization (see the P-E loops and ferroelectric switching in Fig. S12) and the substitution-induced magnetization (see the M-H loops in Fig. 6).

Normally, it is difficult to get the saturated polarization in Aurivillius-phase oxides due to high ferroelectric coercive field, E_c. Although, in Fig. S12, the P-E loops are not saturated, the electrical current peaks in the inset of Fig. S12 evidence the ferroelectric polarization switching. Moreover, Fig. S10 shows the Curie temperatures, T_c, of the Aurivillius compounds, which are, according to the Abrahams-Kurtz-Jamieson relationship (Physical Review, 1968, vol. 172, p. 551), directly related to the spontaneous polarization of ferroelectrics.

Referee 2

Manuscript can be accepted after minor revisions as per the following comments.

Comment 1. Bragg peak positions and space groups should be presented with different colours in Fig. 3.

Figure 3 is redrawn in the revised version, following the referee's comment.

Comment 2. Why composition (x = 0, y = 0.3) was not tried for the study?

In our previous study (Ref. [18], J. Phys. Chem. C 122, 1374-1380), we have demonstrated that the Aurivillius $Bi_{5-x}Gd_xFeTi_3O_{15}$ materials (i.e., without cobalt) are paramagnets from 5 K to 700 K. An introduction of paramagnetic niobium ions cannot give rise to a long-range magnetic order in the Aurivillius phase. Therefore, the (x=0, y=0.3) composition has not been investigated.

Comment 3. Why the Mössbauer spectrum of BiG4 sample was not presented? Is it similar to BiG5 sample?

Because of a very low amount of iron and strong absorption of gamma radiation by bismuth and gadolinium cations, the process of acquiring of ^{57}Fe Mössbauer spectrum and reliable analysis of the obtained data for the samples under investigation are time-consuming and challenging. Hence, aiming at the specific study of the octahedral environment and magnetic hyperfine interactions in the doped samples, Mössbauer spectroscopy has been carried out on the representative samples BiG1, BiG3 (Co added) and BiG5 (co-doping with Co and Nb).

Comment 4. Present the final fitted data (theoretical) in the Mössbauer spectra.

Fig. 5 displays the final fitted data (full red circles). The figure caption is modified in the revised version (page 18) in order to describe all contributions to the measured Mössbauer spectra.

"Figure 5. Fitted room-temperature Mössbauer spectra of BiG1, BiG3 and BiG5 (full red circles – total fit, pink and green doublets – paramagnetic contributions, blue sextet – hyperfine splitting). The inset illustrates the distribution of the hyperfine magnetic field induction for the BiG5 sample."

Comment 5. Figure 7: Match the colour code of inset with main figure data.

Colour of the number representing the magnetic transition temperature of the BiG3 sample in the inset of Fig. 7 is changed from black to blue in the revised manuscript in order to match the colour code of the main figure data.

Comment 6. Write the sample formula in the graphical abstract.

The chemical formula of the representative Aurivillius sample is included in the revised version of the graphical abstract.

Referee 3

I recommend its publication in the journal. I have only one main comment to the autors:

Comment 1. In oxides having Co3+ ions in octahedral environments, normally these ions adopt the LS (S=0) electronic configuration at low temperature. This has not been mentioned nor discussed in the text. The paper presents magnetometry data at low temperatures (Fig. 6, Fig. 10, Fis. S3, S6). Do you see any possible sign of Co3+ ions being in LS (S=0) at low temperature? Could the occurrence of a HS-to-LS transition in Co3+ ions have some relationship with the spin glass-like behavior observed in the Co-doped samples?

As a matter of fact, in the present manuscript, it was not our intention to go deeply into the physics of spin states, spin states transitions, etc., and discuss the observed glassy magnetic behaviour in the Aurivillius phases without proper "first principle" calculations. The detailed study of electronic structures, DOS and spin states is currently running and findings will be the subject of our upcoming publication. Nevertheless, encouraged by the referee's comment, we would be happy to share our thoughts regarding the low-temperature cluster glass state of the Co-doped Aurivillius oxides with the readership of *Journal of Materials Chemistry C*.

Obviously, the authors agree with the referee comment about the low spin (LS) state of Co^{3+} at low temperatures (see, for instance, the paramagnetic behaviour of the ZFC magnetization below 20 K in Fig. 10 and Fig. S6) and possible effect of spin crossover phenomena on the observed spin glass-like behaviour. Additionally, we believe that the valence fluctuation of cobalt, as evidenced by the NEXAFS study, would play an important role in the low-temperature glassy behaviour of the doped samples as well.

Taking this opportunity, the authors added in the revised manuscript (page 14, in Supplementary material) the following:

"From the AC susceptibility analysis, one can infer that the glassy magnetic behavior of the Aurivillius compounds originates from competing antiferromagnetic and ferromagnetic interactions within and between the cooperative Fe-O-Co polar clusters, which support the presence of Co^{3+} ions in the low spin (LS) state, Co^{3+} (S=0). According to Goodenough-Kanamori rules for super-exchange interactions [50], a disordered distribution of LS Co^{3+} and high spin Fe^{3+} would result in the frustration between the ferromagnetic double exchange (Co-Fe) and the antiferromagnetic super-exchange (Co-Co and Fe-Fe) interactions. The presence of low concentrations of Co^{2+}, as indicated by the XAFS study, in the high spin (S=3/2) electronic configuration further rationalize the spin glass behavior at low temperatures, as the HS Co^{2+} - HS Co^{2+}, HS Co^{2+} - HS Co^{3+} interactions are antiferromagnetic [50]."

Comment 2. Better to specify the temperature of the NEXAFS and EXAFS plots in the corresponding captions.

X-ray absorption fine structure (XAFS) spectroscopy measurements were carried out at room temperature. This information is given now in the revised manuscript, i.e. in the captions of Fig. 9 and Fig. S5(a). In addition, the XAFS experiment number and acknowledgement to Dr. Welter for his assistance during the experiment are included in Acknowledgements.

"Figure 9. XANES Fe *K*-edge spectra of the BiG1-BiG5 samples and reference powders of hematite (α-Fe_2O_3) and magnetite (Fe_3O_4), as collected at room temperature. The insets show a zoomed part of spectral peaks A and C."

"Figure S5. (a) The room-temperature XANES Co *K*-edge spectra of the BiG1-BiG5 samples. (b) Fourier transform (FT) of the EXAFS function, $\chi(k)$, into real space for the BiG1-BiG5 samples."

Comment 3. Listed below I report some errors, mistakes or technical concerns that need to be addressed.

-a) NSM (nanoscale structural modulation) has not been defined in the text.

NSM is defined in the revised manuscript (page 4), as follows:

"…reported on the nanoscale structural modulation (NSM) induced by…"

-b) The caption in the Fig. 2 suggests that XRD data were collected at three different "high temperatures". In the experimental section one can read that XRD was performed at room temperature. Make clearer that these temperatures in Fig.2 refer to "processing temperatures".

The caption is fixed in the revised manuscript (page 9), as follows:

"Figure 2. The room-temperature XRD patterns of (a) BiG1, and (b) BiG4, as processed at three different temperatures – 1063 K, 1173 K and 1223 K (upper plot – peak positions of the experimental pattern of the sintered samples and reference main phase(s)/impurity; bottom plot - peak positions of the experimental pattern of the calcined powder and reference intermediate phases)."

-c) Caption of the Fig. 3: the caption should specify that these Rietveld plots correspond to "Profile Matching".

The caption is fixed in the revised manuscript (page 12), as follows:

"Figure 3. Rietveld plot for the refinement (a full-profile matching method) of (a) BFTO, (b) BiG1, (c) BiG2, (d) BiG3, (e) BiG4, and (f) BiG5. The allowed Bragg reflections for the corresponding space groups *A2₁am*, *B2cb* and *I*23 are marked by green, orange and pink ticks, respectively. Black open circles represent the observed data, red solid line is the calculated profile and blue solid line illustrates the difference between the observed and calculated data."

-d) P. 2:   Ruddlesden–Popper" instead of "Ruddleson-Popper"

The name of the phase is corrected in the revised manuscript (page 2), as follows:

"…namely Ruddlesden-Popper, Aurivillius and…"

-e) Pags. 22 and 23: "iron-reach" or "iron-rich" areas?

The error is fixed in the revised manuscript (page 22 and 23), as follows:

"…iron-rich…"

In addition, in the revised manuscript, the presentation in Fig. S7 is improved in order to show tiny impurities ant their EDX spectra markedly.

-f) Some colors in the Fig. 6 are rather similar and difficult to distinguish.

Figure 6 is redrawn in the revised manuscript in order to make plots distinguishable.

 -g) P. 29: "Spectral peaks D and E...".The peak E has not been labelled in fig. 9.

The sentence is modified in the revised manuscript (page 30) and reflects now all the features shown in Fig. 9.

"Spectral feature D results from the multiple-scattering contribution of absorbing Fe in FeO_6 octahedra surrounded by Bi and Gd ions."

Yours sincerely,

Dr. Vladimir Koval (on behalf of the authors)

Cobalt-induced structural modulation in multiferroic Aurivillius-phase oxides

V. Koval[1], Y. Shi[2], I. Skorvanek[3], G. Viola[4], R. Bures[1], K. Saksl[1], P. Roupcova[5,6], M. Zhang[4], Ch. Jia[2], and H. Yan[4]

[1]*Institute of Materials Research, Slovak Academy of Sciences, Kosice, Slovakia*

[2]*Key Laboratory for Magnetism and Magnetic Materials of MOE, Lanzhou University, China*

[3]*Institute of Experimental Physics, Slovak Academy of Sciences, Kosice, Slovakia*

[4]*School of Engineering and Materials Science, Queen Mary University of London, United Kingdom*

[5]*Institute of Physics of Materials ASCR, Brno, Czech Republic*

[6]*CEITEC Brno University of Technology, Brno, Czech Republic*

ABSTRACT

Attaining robust magnetic long-range order in ferroelectric Aurivillius-phase oxides at room temperature has recently attracted considerable attention of material scientists and engineers for the development of magnetoelectric-active materials in microelectronics and spintronics.

Here, we report the structural evolution and its relation to the macroscopic magnetization of the series samples of Aurivillius $(Bi_{4.3}Gd_{0.7})(Fe_{1-x}Co_x)_{1+y}Ti_{3-2y}Nb_yO_{15}$ (x=0, 0.3, 0.5 and y=0, 0.3) compounds prepared by solid state reaction, aiming at shedding light on the Co substitution-induced ferromagnetism at room temperature and above. The Co-free composition showed a single-phase four-layered Aurivillius structure (a space group $A2_1am$), while the Co substitution was found to give rise to a mixed-layer structure composed of four- and three-layered phases. Rietveld analysis of the synchrotron X-ray diffraction data showed that the reduction in the number of layers across the Aurivillius morphotropic transition boundary is accompanied by a structural phase transformation from $A2_1am$ to $B2cb$. The disordered intergrowth of these phases was evidenced by high-resolution transmission electron microscopy and found to originate from a nanoscale structural modulation occurring at the interface between the two phases. A sextet suggesting a long-range magnetic ordering in the doped samples was deduced from Mössbauer spectra. Magnetic-property measurements, indeed, confirmed a ferromagnetic state of these samples at elevated temperatures. The highest values of the remanent and saturation magnetization at room temperature were obtained for the compositions with x=0.3, in which the occurrence and enhancement of the magnetization can be attributed to the ferromagnetic clustering of the FeO_6 and CoO_6 octahedra and, partly, also to the spin canting effects and/or a double-exchange magnetic interaction between the mixed valence cobalt through oxygen. The cooperative freezing of randomly distributed Fe-O-Co clusters is

suggested to be responsible for the spin glass-like behaviour observed at low temperatures. The occurrence and enhancement of the magnetization in the ferroelectric Co-doped Aurivillius ceramics is attributed, respectively, to the NSM and the population of the ferromagnetic clusters nearby the interface of the four- and three- layered phases.

1. Introduction

Today's advanced electronic technologies take advantage of materials with extraordinary electrical and magnetic properties. Among them, perovskite-type ferroelectric magnets or the so called magnetoelectric multiferroics have attracted increasing attention because of their chemical and structural versatility for the fabrication of modern multifunctional devices. The coupling between the ferroelectric and magnetic order parameters in these materials is expected to bring about an extra functionality to tune the electrical properties by a magnetic field or manipulation of the magnetic state by an electrical field via the magnetoelectric effect.[1] The enhanced multifunctionality accompanied by a progressive downscaling of magnetoelectric multiferroics would enable rapid miniaturization of the present solid-state electronics and will open up entirely new possibilities for designing novel applications in microelectronics and spintronics, including four-state nonvolatile memories for high-density, low-power storage digital units and electric-field-controlled ferromagnetic resonance devices.[2,3]

Recently, various approaches of developing novel classes of multiferroic materials created on the basis of layered perovskites, namely Ruddlesden-Popper, Aurivillius and Dion-Jacobson phases have been suggested.[4] Most of them are ferroelectric and the introduction of magnetic ions in perovskite-like layers can give rise to the occurrence of a long-range magnetic order. Owing to their good ferroelectric properties, such as Curie temperatures well above room temperature and low fatigue [5], Aurivillius-family compounds are considered as the most promising candidate for magnetoelectric-active multiferroic materials.[6-8] The Aurivillius phase has the general formula $[Bi_2A_{n-1}B_nO_{3n+3}]$ and structurally is typified by perovskite-like $[A_{n-1}B_nO_{3n+1}]^{2+}$ layers (where n and $n-1$ are the numbers of oxygen octahedra and pseudo-perovskite units in a perovskite-like layer, respectively) stacked along the [001] direction, and separated by fluorite-like layers of $[Bi_2O_2]^{2+}$. Obviously, for $n=\infty$, the Aurivillius-phase structure is equivalent to a perovskite structure.

A number of iron-containing Aurivillius oxides with the general formula $Bi_{n+1}Fe_{n-3}Ti_3O_{3n+3}$ ($n\geq4$) have been investigated for possible multiferroic properties and spin-orbit interaction-driven magnetoelectric coupling.[9-16] As it has turned out, the introduction of

magnetic Fe ions into perovskite blocks, even at higher concentrations (for n=5-8), does not lead to a long-range ferromagnetic order in ferroelectric Aurivillius-phase materials at room temperature.[10-12] Compounds such as $Bi_5FeTi_3O_{15}$, $Bi_6Fe_2Ti_3O_{18}$, and $Bi_9Fe_5Ti_3O_{27}$ were reported to be antiferromagnetic with their Néel temperatures increasing from 80 K (n=4) to 270 K (n=8).[13-16] Though, Srinivas et $al.$ [14,15] observed at 300 K a small ferromagnetic hysteresis in the field-dependent magnetization (M-H) loops of the $Bi_7Fe_3Ti_3O_{21}$ and $Bi_8Fe_4Ti_3O_{24}$ compounds, suggesting a weak room temperature ferromagnetism. By employing new theoretical and experimental approaches [11,17,18,19], it has been recently demonstrated that most of the multi-layered Aurivillius materials, including $Bi_5FeTi_3O_{15}$ (BFTO), are paramagnets at room temperature and the weak magnetic signals are brought by trace amounts of secondary phases, such as Fe-rich or Co-rich spinel-type impurities, which are magnetic but extremely hard to detect using standard laboratory-based characterization techniques. Despite the absence of magnetic long-range order at room temperature, a ferroelectric BFTO was reported to exhibit a strong magnetoelectric coupling.[10,13,20] Zhao et $al.$ [10] suggested that a high value of the linear magnetoelectric coefficient ($\alpha \sim 400$ mVOe^{-1}cm^{-1}) of the BFTO films originates from short-range magnetic ordered Fe-rich nanoregions, in which the canting of antiferromagnetically coupled Fe spins gives rise to a robust magnetoelectric coupling through the Dzyaloshinskii-Moriya interaction (DMI). While doping at the A-site by rare earths with smaller ionic radius than the Bi^{3+} ion was found to improve the ferroelectric properties, as a consequence of the reduced oxygen vacancies [21,22], a partial replacement of Fe^{3+} ions at B-sites by the isovalent Co ions resulted in the room-temperature spontaneous magnetization of BFTO [22,23]. A ferromagnetic coupling over Fe-O-Co octahedral clusters was suggested by Mao et $al.$ [23] to be responsible for the observed magnetization of $Bi_5Fe_{0.5}Co_{0.5}Ti_3O_{15}$. Wang et $al.$ [24] studied the effect of the Co concentration on multiferroic properties of the sol-gel prepared $Bi_5Fe_{1-x}Co_xTi_3O_{15}$ (x=0-0.25) thin films and found that the x=0.12 composition shows the highest value of the remanent magnetization (M_r=0.42 emu.cm^{-3}). For the Co-substituted BFTO ceramics (BFCT), they obtained the highest remanent magnetization (2M_r=7.8 memu.g^{-1}) at x=0.5.

It was reported that the magnetization of BFCT can be further enhanced by rare earth doping at the A-sites.[25-29] Zuo et $al.$ [28] suggested three different factors, which could possibly contribute to the improved ferromagnetism in Gd-doped BFCT: (i) a large magnetic moment of Gd^{3+}, (ii) enhancement in exchange interactions of Co^{3+}-O-Fe^{3+} driven by Gd-substitution induced suppression of oxygen vacancies, and (iii) structural distortion induced by the mismatch of ionic sizes of Bi^{3+} and Gd^{3+}. It should be mentioned that an opposite tendency

3

is typically observed for the magnetization (ferromagnetism) and polarization (ferroelectricity) of BFCT-derived compounds against the Co doping. With the increasing Co concentration the ferroelectric polarization of the layered perovskite-like Aurivillius materials diminishes due to the increased leakage currents, whereas the magnetic moment increases.[26,28,30]

Apparently, the method of the A-site rare-earth ion doping combined with the B-site $3d$-transition metals co-substitution (e.g., the Fe/Co co-substitution) is an effective way to optimize ferromagnetic and ferroelectric properties of the bismuth-layered Aurivillius phases, and obtain a single phase multiferroic material displaying large magnetoelectric coefficient at room temperature. Our recent studies on the room-temperature multiferroic properties of the La-doped three- and four- layered BFCT compounds have proven the efficacy of this strategy, by yielding a single phase multiferroic material with the intrinsic magnetoelectric coupling at room temperature.[8,22]

To address the most compelling question on the origin of ferromagnetism in Co-substituted BFTO-derived compounds, we prepared polycrystalline samples in the $Bi_{4.3}Gd_{0.7}(Fe_{1-x}Co_x)_{1+y}Ti_{3-2y}Nb_yO_{15}$ (x=0, 0.3, 0.5 and y=0, 0.3) series and investigated the effect of the cobalt substitution on the crystal chemistry and macroscopic magnetization of these Aurivillius materials. Very recently, Sun *et al.* [31] have reported on the nanoscale structural modulation (NSM) induced by Co-substitution in the Aurivillius oxide of $Bi_{11}Fe_3Ti_6O_{33}$, which resulted in a mixed-layer structure composed of four- and five- layered phases. The disordered intergrowths of Aurivillius phases with different number of pseudo-perovskite layers in slabs have been confirmed to exist in the mixed-layer structures of $Bi_4NdFe_{1-x}Co_xTi_3O_{15}$ [29] and $Bi_7Fe_{3-x}Co_xT_3O_{21}$ [32]. Furthermore, it has been demonstrated that the magnetization as well as ferroelectric properties of these materials can be significantly improved at a certain doping level of Co, corresponding to the Aurivillius morphotropic transformation (AMT) composition.[31] In the present work, we carried out a comprehensive structural analysis of the perovskite-like Aurivillius phase multiferroics in order to evaluate the substitution-induced structural evolution in the phase-modulated samples, and subsequently correlate changes in their magnetization behaviour.

2. Experimental

2.1 Sample preparation

A conventional solid state reaction method was employed to prepare the polycrystalline $Bi_{4.3}Gd_{0.7}(Fe_{1-x}Co_x)_{1+y}Ti_{3-2y}Nb_yO_{15}$ compounds, hereafter denoted as BiG1 (x=0, y=0), BiG2

(x=0.3, y=0), BiG3 (x=0.5, y=0), BiG4 (x=0.3, y=0.3), and BiG5 (x=0.5 and y=0.3). After drying at 420 K for 3 h, the stoichiometric amounts of the constituent oxide powders Bi_2O_3, Gd_2O_3, Fe_2O_3, Co_3O_4, Nb_2O_5 and TiO_2 (all from Sigma-Aldrich, purity ≥99.99%) were thoroughly mixed for 2 h, using a planetary ball mill, in a polyamide mortar filled with ZrO_2 milling balls and isopropyl alcohol as a liquid medium. The slurry was dried and, then, the powder mixture was calcined in an alumina crucible in two steps. Firstly, the powder was heated to 1063 K at a rate of 300 K h^{-1} with a 4 h dwell at temperature followed by cooling down to room temperature naturally. The pre-calcined product was crushed and then milled again in the planetary mill for another 1 h. In the second step, the powder precursor was calcined at 1123 K for 4 h. The calcined powders were pressed into pellets (diameter ~12 mm, thickness ~2 mm) at 150 MPa followed by sintering at a range of different temperatures (1173-1273 K) in order to optimize the density of pellets. The maximum sintered density of about 7.49 g cm^{-3} (~94% of the theoretical density), as obtained by the Archimedes method, and crack-free microstructures were obtained for the samples sintered at 1223 K for 5 h. The heating rate was set again to 300 K h^{-1}. During sintering, the pellets were kept in a sealed alumina crucible in order to reduce volatilization losses due to an excessive evaporation of bismuth at high temperatures.

2.2 Phase and (crystal and electronic) structure characterization

Kinetics of the formation of the Aurivillius phases and the ferroelectric transition-induced changes in their thermal behaviour were investigated by differential thermal calorimetry (DSC) and thermogravimetry (TG), using a DTA-DSC-TG analyzer (Jupiter STA 449-F14, NETZSCH, Germany), in air at a controlled heating/cooling rate of 300 K h^{-1}. Phase analysis and characterization of the crystal structure were performed at room temperature by X-ray diffraction (XRD) using Cu K_α radiation (Philips X'Pert Pro diffractometer, PANalytical, Netherlands) and a monochromatic synchrotron radiation of photon energy 76.01 keV (the beamline I15 at the Diamond Light Source, Didcot, Oxfordshire, UK). The room-temperature Raman spectra were collected in back-scattering geometry using a LabRam micro-probe system (ISA/Jobin-Yvon/Horiba, France) with the 488 nm Ar^+ laser excitation. Full details on the XRD and Raman scattering data acquisition, processing and analysis are given elsewhere.[18] ^{57}Fe Mössbauer spectra were collected by a standard transmission method at room temperature using a ^{57}Co/Rh source. The calibration of the spectra is referred relative to α-Fe at room temperature. The computer processing of the spectra was done by the CONFIT package [33] yielding the

intensities of the components (atomic fraction of Fe atoms), their hyperfine field, isomer shift and quadrupole splitting. The X-ray absorption fine-structure (XAFS) measurements were performed at the beamline P65 located at the PETRA III synchrotron storage ring. Spectroscopic data in the range of 6960-7912 eV were collected in fluorescence mode using a fixed-exit double-crystal Si(111) monochromator. During all XAFS measurements, the samples were irradiated by an X-ray beam with a cross-section of 2x0.4 mm (width x height). The X-ray intensities were monitored using ionization chambers filled by nitrogen (18% absorption). The fluorescence detector (Passivated Implanted Planar Silicon, PIPS) was placed approximately 10 cm away from the sample and at an angle of 45^0 with respect to the incoming X-ray beam. The experimentally measured X-ray absorption cross sections, $\mu(E)x$, were analyzed using the FEFF 9.01 [34].

2.3 Microstructure and atomic-resolution imaging

The scanning electron microscopy (SEM) and energy dispersive X-ray (EDX) analysis were carried out on mirror-polished and thermally etched samples using a cold field-emission microscope (JSM 7000F, JEOL, Japan) equipped with an EDX spectrometer (Oxford Instruments, UK). Atomic resolution high angle annular dark field (HAADF) images from the electron transparent ready samples were taken by an aberration corrected FEI Titan Themis 300 microscope operated in scanning transmission electron microscopy (STEM) mode.

2.4 Magnetic property measurements

Magnetic properties at low temperatures and elevated temperatures, including room temperature were measured by using a magnetic properties measurement system (model MPMS-XL-5, Quantum Design, USA) equipped with a superconducting quantum interference device (SQUID) magnetometer and a vibrating sample magnetometer (VSM) unit (model EV9, MicroSense, USA), respectively.

3. Results and discussion

3.1 Phase composition analysis

Thermal analysis

Fig. 1(a) displays the differential thermal calorimetry (DSC) curves recorded for the BiG5 composition powder sample upon heating, curve DSC(1), and cooling, curve DSC(2), in the temperature range of 780-1350 K. While the differential thermogram DSC(1) provides

information on the kinetics of the formation of layered perovskite-like compounds from temperatures well below calcination up to those above the sintering temperature, the thermal events occurring on the DSC(2) curve reflect the specific physical quantities of the Aurivillius polycrystalline material. The endothermic peaks at a temperature of about 1308 K and 1095 K can be attributed to the melting point and the ferroelectric Curie point, respectively, of the $(Bi_{4.3}Gd_{0.7})(Fe_{0.5}Co_{0.5})_{1.3}Ti_{2.4}Nb_{0.3}O_{15}$ compound. Fig. 1(b) shows the Curie temperatures (T_c^{FE}) of all the compositions under investigation. From the figure, it is clear that the endothermic peak corresponding to the ferroelectric phase transition shifts to lower temperatures as the amount of the substituting Co ions increases. Similar trend in the phase transition behaviour is observed upon Co/Nb- codoping. The ferroelectric T_c is decreased by ~10 K, from about 1106 K (BiG1) to about 1095 K (BiG5), once the initial $Bi_{4.3}Gd_{0.7}FeTiO_3$ system is modified at the Fe sites by Co (x=0.5) and simultaneously at the Ti^{4+} sites by Nb (y=0.3). It should be mentioned that the T_c^{FE} of BiG1 is in close agreement with the values of rare-earth-doped BFTO Aurivillius multiferroics reported in the literature [22,28], and correlates well with the results of our dielectric study discussed in the following section.
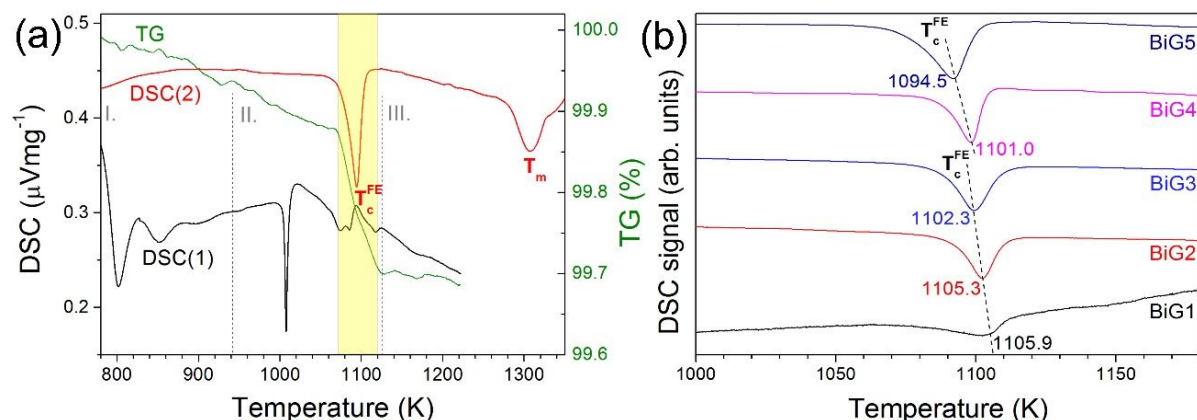

Figure 1. (a) DSC curves of the BiG5 composition samples. Reaction kinetics of raw oxides upon heating, curve DSC(1) - black line, and TG curve – green line. Thermogram of the reacted powder upon cooling, curve DSC(2) - red line, with two distinct thermal events. (b) Ferroelectric phase transition temperatures of the BiG1-BiG5 samples, ferroelectric Curie temperatures, T_c^{FE}, as determined from the DSC curves.

In Fig. 1(a), three main thermal regions (I, II and III) are clearly distinguishable upon heating of the stoichiometric mixture of the raw oxides up to 1275 K (curve DSC(1)), suggesting a multi-stage synthesis process similar to the formation of Aurivillius phases in the Bi_2O_3-TiO_2-Fe_2O_3 system previously reported [35]. According to the proposed scheme, the

low-temperature region 775-915 K can be linked with the formation of intermediate Bi_2O_3-reach compounds, namely $Bi_{12}TiO_{20}$ and a compound close in composition to $Bi_{24}Fe_2O_{39}$. These sillenite-type phases are crystallochemically related to γ-Bi_2O_3; they adopt a cubic structure (space group, SG: $I23$) with almost identical cell parameters [36]. Their transformation can be considered as a phase transition α-$Bi_2O_3 \rightarrow \gamma$-$Bi_2O_3$ initiated by incorporation of a small amount of titanium and iron dioxide admixtures into the Bi_2O_3 structure. The endothermic peaks at about 801K and 850 K are close to the melting point of the γ-Bi_2O_3-based surface phase (T_m^{surf} $\approx$823-853 K [37]) at which the two solid-state reactions (α-$Bi_2O_3 \rightarrow Bi_{12}TiO_{20}$ and α-$Bi_2O_3 \rightarrow Bi_{24}Fe_2O_{39}$) are supposed to take place very fast. It has been reported that the α-$Bi_2O_3 \rightarrow Bi_{12}TiO_{20}$ transformation, which does not require changes in chemical bonds nor significant activation of the mass transfer (only 1 mol of TiO_2 should be incorporated per 12 mol of $BiO_{1.5}$ units), occurs readily, leading to the formation of the $Bi_{12}TiO_{20}$ sillenite at temperatures slightly below the melting points of the non-autonomous phases in the Bi_2O_3-TiO_2 system.[35] With increasing the temperature, the mass transfer is accelerated, reaching its maximum (limited by the rate transport processes) at temperatures close to the melting point of the surface phase based on $Bi_{12}TiO_{20}$ [37] and both polymorphic transformations $\alpha \rightarrow \gamma$ of $Bi_{24}Fe_2O_{39}$ [38] and $\alpha \rightarrow \delta$ of $Bi_{24}Co_2O_{39}$ [39] (endothermic peak at T=1007.5 K). The endothermic peaks at about 1074 K and 1085 K can be ascribed to the peritectic transformations γ-Bi_2O_3+liq.$\leftrightarrow Bi_{24}Fe_2O_{39}$ and δ-Bi_2O_3+liq.$\leftrightarrow Bi_{24}Co_2O_{39}$, respectively [38,39]. All these processes in the intermediate thermal region (region II) facilitate the formation of the $GdFeO_3$-like phase, i.e., an orthorhombically distorted ABO_3-type perovskite with the Gd and Bi ions occupying the A sites of the ABO_3 unit, while the $3d$ metals (Fe^{3+} and Co^{3+}) enter the octahedrally coordinated B sites. On the thermogravimetric (TG) curve (green line, Fig. 1(a)), one can see a rapid drop in the mass loss (Δm=-0.19%) between 1074 K and 1085 K, manifesting the formation of the perovskite-type phases. This decrease in the mass represents more than 60% of the total mass loss (Δm=-0.31%) during the heat treatment over the temperature window 775-1225 K. As the temperature increases further, the $Bi_{12}TiO_{20}$-based surface phase starts to melt (the melting point of $Bi_{12}TiO_{20}$ is 1148 K [37]), leading to formation of the $Bi_4Ti_3O_{12}$ (BTO) Aurivillius phase (endothermic peak at T$\approx$1118 K). In the high-temperature region III, the thermally-induced rearrangement and transport processes associated with the incorporation of the perovskite $GdFeO_3$-type units into the three-layered BTO-like structure give rise to the four-layered Aurivillius phase of $(Bi,Gd)_5(Fe,Co,Ti,Nb)_4O_{15}$. SEM analysis of the microstructure revealed that the Co substitution and Co/Nb- codoping can

effectively promote the grain growth in the polycrystalline Aurivillius samples (see Supplementary material).
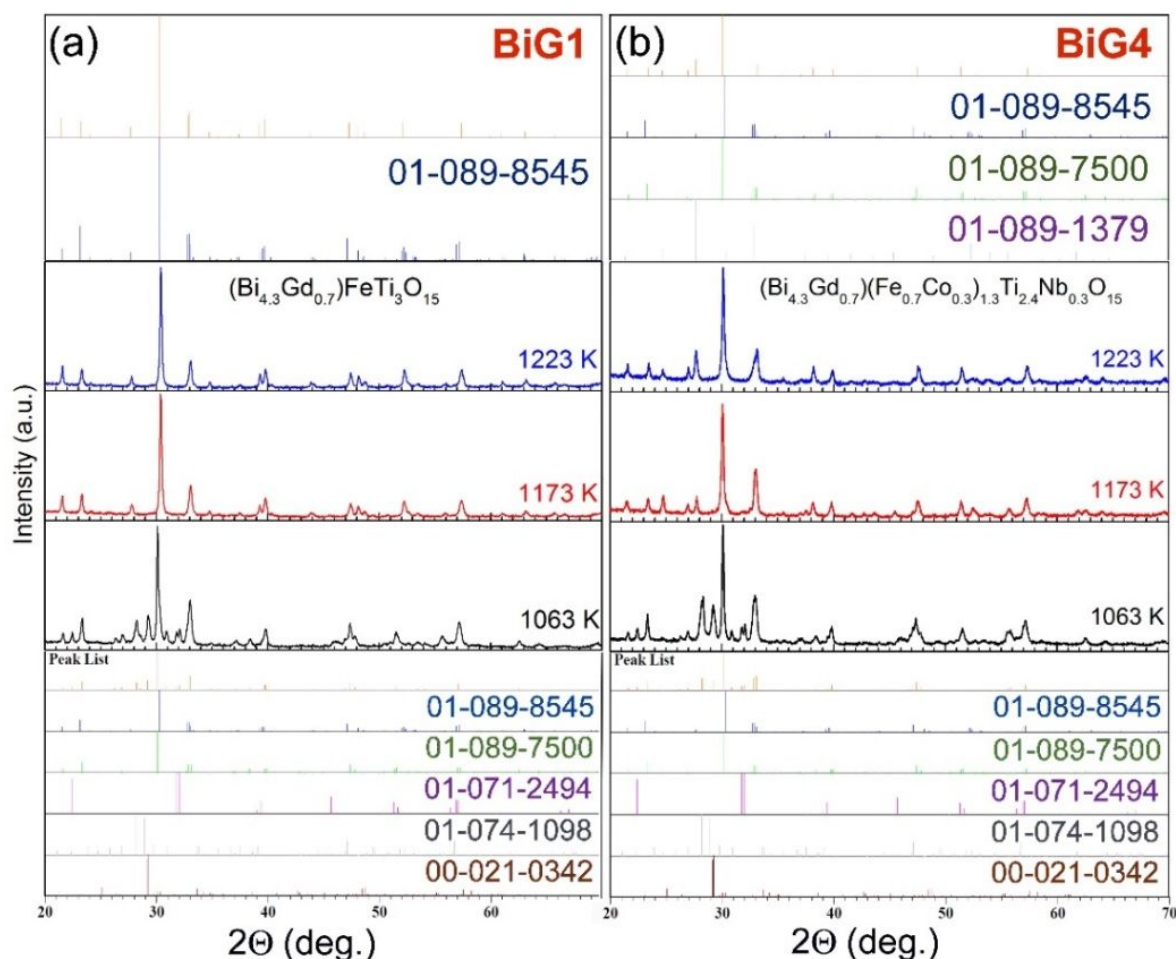
X-ray phase match analysis

Figure 2. The room-temperature XRD patterns of (a) BiG1, and (b) BiG4, as processed at three different temperatures – 1063 K, 1173 K and 1223 K (upper plot – peak positions of the experimental pattern of the sintered samples and reference main phase(s)/impurity; bottom plot - peak positions of the experimental pattern of the calcined powder and reference intermediate phases).

In order to confirm the proposed scheme of the phase evolution and investigate the phase composition at certain stages of material processing, the qualitative XRD analysis of crystal structures of the calcined and sintered powders has been performed. Figs. 2(a) and 2(b) show the representative XRD patterns along with the most significant phases (>5%) identified for the BiG1 and BiG4 composition systems, respectively, by a search-and-match analysis of the mixed

9

powders calcined at 1063 K and sintered at 1173 K and 1223 K. The results of whole-profile matching simulation of the XRD data for both systems are given in Table 1.

Table 1. Phase composition of the selected samples.

Sample/ structural phase	Phase fraction (%) at processing temperatures:			
	1063 K	**1123 K**	**1173 K**	**1223 K**
BiG1				
4-layered Aurivillius (BFTO-like)	6.7	32.5	71.5	100
3-layered Aurivillius (BTO-like)	49.0	33.4	10.5	
Perovskite-type ($BiFeO_3$)	8.5	-	-	
Perovskite-type ($GdFeO_3$)	10.8	18.9	5.2	
Mullite-type ($Bi_2Fe_4O_9$-like)	15.9	6.6	5.5	
Other intermediate phases (< 5%)	9.1	8.6	7.3	
BiG4				
4-layered Aurivillius (BFTO-like)	9.2		6.6	16.8
3-layered Aurivillius (BTO-like)	28.3		34.7	74.3
Perovskite-type ($BiFeO_3$)	5.0		12.3	
Perovskite-type ($GdFeO_3$)	19.9		9.8	
Mullite-type ($Bi_2Fe_4O_9$-like)	14.6		14.3	
Sillenite-type ($Bi_{12}TiO_{20}$-like)	-		6.4	8.9
Unreacted Gd_2O_3	13.2		8.4	
Other intermediate phases (< 5%)	9.8		7.5	

From the table, one can see that sintering of the BiG1 sample at 1223 K results in single-phase material with the crystal structure resembling that of the four-layered $Bi_5FeTi_3O_{15}$ Aurivillius phase (JCPDS Card No. 01-089-8545, [36]). The orthorhombic structure (SG: $A2_1am$) in the sample develops in stages as described in the previous section; after calcination at 1063 K for 2 h, the powder sample consists of a large fraction of an orthorhombic $Bi_4Ti_3O_{12}$-like phase (JCPDS Card No. 01-089-7500) and a reaction by-product structurally similar to the mullite-type $Bi_2Fe_4O_9$ compound (JCPDS Card No. 01-074-1098). The amount of the four-layered Aurivillius phase with the structure close to BFTO was found to be less than 10%. Partially, the perovskite-type phases, such as $BiFeO_3$ (JCPDS Card No. 01-071-2494) and $GdFeO_3$ (JCPDS Card No. 01-078-0451), are present in the calcined material (~10% each), as expected. Small portions of the sillenite $Bi_{24}Fe_2O_{39}$ (JCPDS Card No. 00-042-0201), Gd_2TiO_5 (JCPDS Card No. 00-021-0342) and unreacted gadolinium oxide (JCPDS Card No. 01-043-1014) were identified in the diffractogram, but their contribution, as individual constituents, to the fitted profile was less than 5%. Similar phase composition was identified in the calcined BiG4 sample. Surprisingly, the situation for the Co-doped and undoped $Bi_{4.3}Gd_{0.7}FeTi_3O_{15}$

10

solid-solution systems becomes completely different if one runs processing temperature over the melting point of $Bi_{12}TiO_{20}$. While in BiG1 (sintered at 1173 K) the four-layered BFTO-like phase is the predominant structure (>70%), the fraction of the three-layered Aurivillius phase is more than 3 times larger than that of the BFTO-like phase in the Co-doped samples. It is worth mentioning that the sillenite $Bi_{12}TiO_{20}$ (JCPDS Card No. 01-089-1379) was not detected in BiG1 at all the processing temperatures (within the XRD resolution), whereas it was present in the Co-doped samples sintered at 1173 K. The amount of other intermediate synthesis products is, in general, decreased in both compositions and represents less than 20% of the total XRD signal. At 1223 K, the process of the phase formation is completed for all the compositions yielding the four-layered single-phase BiG1 and the mixed-layer (four- and three- layered) Co-doped (BiG2-BiG5) samples with a small amount of the $Bi_{12}TiO_{20}$-type secondary phase.

As can be seen in Table 2, the content of the cubic impurity is coupled with the ratio of the Fe and Co cations. It slightly increases with increasing the amount of the Co added and its contribution to the XRD pattern reaches about 7.4% for x=0.5 (BiG3). The B-site Co-doping of $Bi_{4.3}Gd_{0.7}FeTi_3O_{15}$ is also accompanied by the decrease in portion of the four-layered Aurivillius phase in favour of the three-layered BTO-like phase. The XRD profile contribution of the BFTO-like structure decreases from 100% in BiG1 to about 70% in BiG3, which is accompanied by the appearance of the three-layered Aurivillius BTO-like phase at even a very low concentration of the Co^{3+} ions (x=0.3) which grows slowly upon further doping. These synthesis effects are more pronounced in the compositions where the Ti^{4+} ions are partially substituted by the Nb^{5+} ions (BiG4 and BiG5). The Nb B-site doping reverses the fraction ratio of the Aurivillius phases in favour of the three-layered BTO-like structure (portion of the three-layered phase in BiG4 and BiG5 is larger than 75%). In the Co/Nb- codoped samples, the BFTO-like structure is the minor phase and contributes less than 20% to the whole profile. It should be also noted that the amount of the secondary phase is slightly higher in the BiG4 and BiG5 samples.

Table 2. Phase composition of the samples sintered at 1223 K.

Sample	Phase fraction (%)		
	4-layered Aurivillius phase	**3-layered Aurivillius phase**	**$Bi_{12}TiO_{20}$-like phase**
BiG1	100	-	-
BiG2	73.5	19.6	6.9
BiG3	71.4	21.5	7.4
BiG4	16.8	74.3	8.9
BiG5	13.6	76.7	9.7

11

The results of the semi-quantitative analysis of the phase composition indicate that the partial substitution of iron ions with the isovalent cobalt ions and further replacement of a part of the Ti^{4+} ions by the donor Nb^{5+} ions in the $Bi_{4.3}Gd_{0.7}FeTi_3O_{15}$ compound induce the transformation of the four-layered BFTO-like phase to the mixed-layer Aurivillius phase. It should be emphasized that the B-site doping makes the synthesis of the BFTO-derived compounds more difficult because these Aurivillius-type oxides are formed in several stages, and due to their low thermal stability they are susceptible to the formation of secondary phases.

3.2. Structural analysis
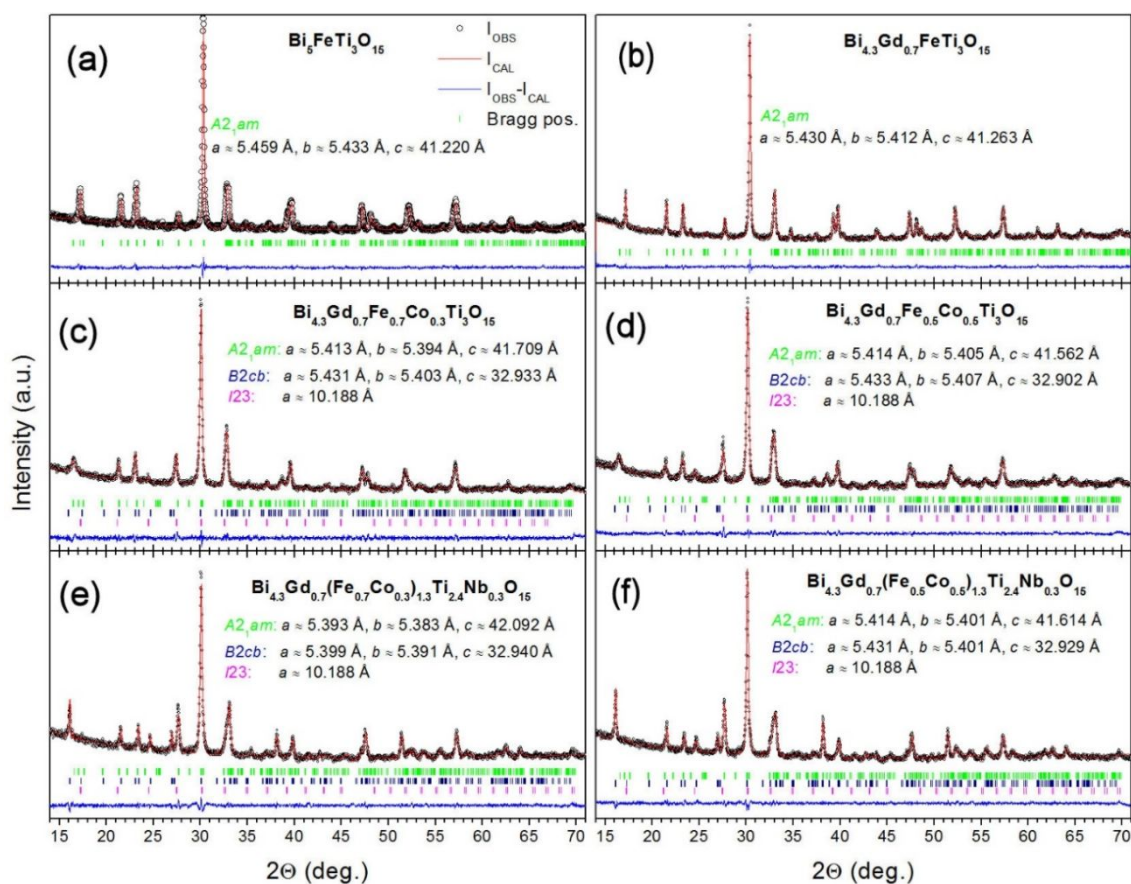
X-ray diffraction analysis

Figure 3. Rietveld plot for the refinement (a full-profile matching method) of (a) BFTO, (b) BiG1, (c) BiG2, (d) BiG3, (e) BiG4, and (f) BiG5. The allowed Bragg reflections for the corresponding space groups $A2_1am$, $B2cb$ and $I23$ are marked by green, dark blue and pink ticks, respectively. Black open circles represent the observed data, red solid line is the calculated profile and blue solid line illustrates the difference between the observed and calculated data.

Detailed Rietveld analysis of the room-temperature XRD data (see Fig. S1 in Supplementary material) confirmed that three phases, including the four-layered orthorhombic phase (SG no. 36: $A2_1am$), the three-layered orthorhombic phase (SG no. 41: $B2cb$) and the sillenite-type cubic phase (SG no. 197: $I23$) coexist in both the Co-doped and Co/Nb- codoped $Bi_{4.3}Gd_{0.7}FeTi_3O_{15}$. The room-temperature XRD patterns of the undoped $Bi_{4.3}Gd_{0.7}FeTi_3O_{15}$, the Co-doped and Co/Nb- codoped samples with data refined by the Rietveld method using full-profile matching are shown in Fig. 3.

As shown in Fig. 3(a) and Fig. 3(b), the single four-layered orthorhombic phase can be clearly distinguished in both the pure and the Gd-doped BFTO samples, confirming no substantial structural effect of the A-site Gd-substitution [18]. The structure of BFTO can be described as a stack of perovskite slabs containing four layers of corner sharing perovskite-like $(Ti/Fe)O_6$ octahedra with Bi^{3+} ions located at the A site, which are separated by the fluorite-type bismuth oxide layers. The partial replacement of the Bi^{3+} ions by the isovalent, but smaller Gd cations (Gd^{3+} ions $r = 1.24$ Å in 12-fold coordination, CN = 12 [40], Bi^{3+} ions $r = 1.31$ Å, CN = 12 [41]), introduces only a slight volume shrinkage of the Aurivillius unit cell ($\approx 0.8\%$), which is associated with a tiny shortening ($\approx 0.4 - 0.5\%$) of both the a and b cell distances and 1% increase in the c-parameter. The refined lattice constants together with the corresponding values of the goodness of fit (GOF) for all the samples are summarized in Table S1.

The incorporation of a small amount of the Co^{3+} ions into the perovskite-like slabs results in the occurrence of the three-layered $B2cb$ Aurivillius phase alongside the initial four-layered phase (Fig. 3(c)). While the dimensions of the $B2cb$ unit in the a-b plane are smaller but still comparable to these of the $A2_1am$ structure, the c-parameter is understandably much smaller than that of the four-layered phase. As the Co concentration is increased to x=0.5 (Fe/Co=0.5/0.5), the lattice parameters a and b further decrease, while c increases in both four- and three- layered phases possibly due to the Jahn-Teller distortion. However, the opposite trend is observed in the unit cell volumes. While the $A2_1am$ lattice expands, the unit cell volume of the $B2cb$ phase slightly decreases with increasing cobalt concentration. This behaviour is even more evident in the samples where niobium is used to partially replace titanium at B sites. From Table S1, one can see that the unit cell volume of the four-layered phase increases from $V \approx 1212$ Å^3 to $V \approx 1222$ Å^3 when the Fe^{3+} and Ti^{4+} ions are substituted simultaneously by the Co^{3+} (x=0.5) and Nb^{5+} (y=0.3) ions, respectively. On the other hand, the volume of the $B2cb$ unit cell of BiG3 drops down from about $V=966$ Å^3 to $V=958$ Å^3 upon the Nb doping (BiG5).

13

In order to investigate the local environment of the B-site cations (Fe, Co, Ti, Nb) in the $A2_1am$ and $B2cb$ phases with a higher accuracy, we employed a high-energy synchrotron X-ray diffraction technique. The results obtained by the Rietveld analysis of the synchrotron XRD data for the BiG1 and BiG4 samples are presented graphically in Fig. S2, and the selected refined structural parameters are summarized in Table S2. From Table S2, one can see that the octahedral tilt along the c-axis in the inner and outer perovskite slabs of the four-layered structure is smaller (9.1^0 and 6.7^0, respectively) than that of the three-layered phase (9.4^0 and 6.9^0, respectively). The increased octahedral tilting can be explained by larger mismatch strains in the doped samples (see Suplementary material).

The refinement results are consistent with our findings about the Co substitution-induced reduction in the number of perovskite-like layers and transformation of the space group of the parent four-layered Aurivillius compound, as obtained from the phase composition analysis, and suggest that the doped samples have the mixed-layer structure composed of the four- and three- layered phases. Zhang *et al.* [29] have recently reported a gradual transformation of four-layered parent phase to three-layered phase induced in a structurally similar four-layered Aurivillius material (Nd-substituted BFTO) by Co doping. The phase evolution, or the so called intergrowth phenomenon has also been observed in six-layer-structured $Bi_7Fe_{3-x}Co_xTi_3O_{21}$, which undergoes a phase evolution from six-layers to four-layers when the concentration of cobalt in the B-site increases from 0 to 1.[32] Sun *et al.* [32] demonstrated using high-resolution transmission electron microscopy that the mixed-layer structure in Aurivillius-type oxides is an inhomogeneous phase with disordered intergrowths of perovskite slabs with different number of layers. They found that the transformation between four- and six-layered phases in the Co-doped $Bi_{11}Fe_3TiO_{33}$ compound is generated from a special shift which occurs at some fluorite-type $(Bi_2O_2)^{2-}$ layers and gives rise to the nanoscale structural modulation at the interface of the two phases. The mixed-layer structure can be, thus, considered as a single phase, similar to a structural modulation widely studied in long-period super-lattice structures such as PZT or PMN with the morphotropic phase boundary (MPB). In our Co-doped samples, both the coexistence of the four- and three- layered phases and substitution-induced structural evolution suggest the possible existence of the NSM. The reduction in the number of layers across the Aurivillius morphotropic transition boundary is accompanied by local phase transformation from $A2_1am$ to $B2cb$. Considering the enhancement effect of the MPB on the dielectric, piezoelectric and ferroelectric properties of simple-structured perovskite oxides, it is reasonable to expect that the 1D phase modulation accompanied by the AMT effect would influence not only the crystal structure (octahedral

14

tilting and lattice distortions) but also the electronic structure and the resulting magnetic and electrical properties of the intergrowth BiG2-BiG5 Aurivillius-phase materials.

Raman spectra analysis

Raman scattering spectra of the Co-free (BiG1), Co-doped (BiG2 and BiG3) and Co/Nb-codoped samples were collected and analyzed in the frequency range of $50 - 1000$ cm^{-1} to get more explicit insights on the structural evolution induced in the Aurivillius phases upon Co doping. In our earlier study [18], it was demonstrated that Raman spectroscopy is a powerful tool for probing local structural distortions and cooperative ionic displacements in bismuth ferrite-derived multiferroics and Aurivillius-phase compounds. Since Raman scattering is capable of exploring short-range structural order, it seems legitimate to employ this technique to investigate structural changes over a few unit cells, if any, in the doped Aurivillius samples.
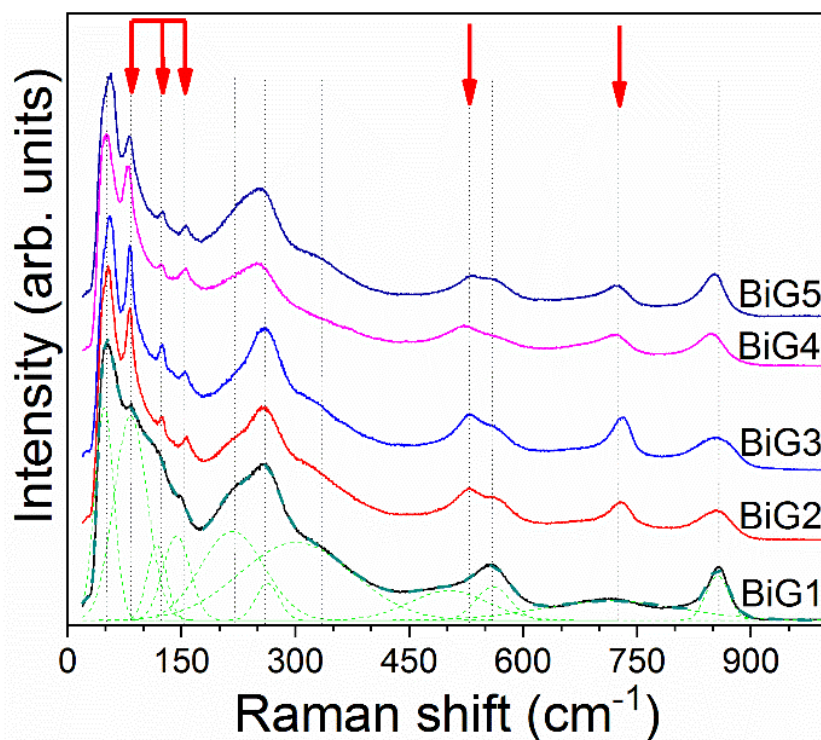

Figure 4. Stacked plot of Raman scattering spectra of the BiG1-BiG5 samples, as collected at room temperature (most significant changes induced by the substitution are marked by red arrows).

Fig. 4 shows the room-temperature first-order Raman spectra stacked and grouped by the composition of the samples (BiG2 and BiG4 with x=0.3; BiG3 and BiG5 with x=0.5; BiG4 and BiG5 are samples with the additional Nb doping at B-sites, y=0.3). At first sight, one can

15

notice that the measured spectra undergo substantial changes upon doping. While the spectral profile of BiG1 resembles the characteristic first-order vibrational modes of the orthorhombic $A2_1am$ phase (details on peak assignment are given in Ref. [18]), a pair of additional low-frequency Raman active modes in between 120-150 cm^{-1} is clearly seen in the spectra of the Co-doped samples, and, concurrently, two phonon modes at around 560 cm^{-1} and 725 cm^{-1} grow substantially with increasing the cobalt content. According to the Raman study on Co/Ni-codoped Aurivillius compounds [42], the enhancement of the latter two modes can be ascribed to the torsional bending and stretching vibrations of the increased amount of the CoO_6 octahedra in the perovskite layers and/or the higher fraction of an orthorhombic phase with lower lattice symmetry (e.g., $B2cb$). A close inspection of the spectral profiles in the high-frequency region (above 200 cm^{-1}) reveals that the internal modes related to the bending, stretching and torsion of the Ti/FeO_6 octahedra in the Co-doped samples coincide well with those of the Co-free sample, indicating that the mixed-layer structure in BiG2 and BiG3 is predominantly formed by the four-layered phase, which is in good agreement with the XRD results. On the other hand, in the Co/Nb- codoped samples, there is a distinct red-shift of the Raman bands at ~260 cm^{-1}, ~560 cm^{-1} and ~850 cm^{-1}, which implies that the heavier niobium atoms replace the titanium atoms, rather than iron atoms at the B-sites of the perovskite units.

Due to the substitution-induced change in the strength of Bi-O bonds (see Table S2), the overlapped stretching modes of the TiO_6 and FeO_6 groups observed in BiG1 as a wide peak centered at 560 cm^{-1} tend to split to a double peak on Co/Nb doping. For the four-layered BFTO, the lower frequency phonon mode (left side of the double peak) has been assigned to the stretching vibrations of the TiO_6 octahedra and that on the right side to the vibrations of the FeO_6 octahedra.[18] In our Co-doped samples (BiG2 and BiG3), the spectral intensity of the lower mode (~529 cm^{-1}) increases with the increasing Co concentration, which can be likely attributed to the progressive overlapping of the vibrational modes from both the TiO_6 and CoO_6 octahedra. It is worth mentioning that the introduction of Nb^{5+} ions at B-sites of the perovskite units suppresses the 560 cm^{-1} Raman band, particularly, the lower frequency mode due to the disordered distribution of Nb cations over the Ti sites. In general, the variety of environments induced within the pseudo-perovskite layers by a random occupation of the octahedral sites with the different cations (Ti, Fe, Co and Nb) is clearly demonstrated in Fig. 4 by the broadness of the Raman bands above 200 cm^{-1}, relative to the vibrational modes of the A-site cations. The broadening effect is even more evident when the Raman profiles of the Co-doped and Co/Nb-codoped samples, for instance BiG3 and BiG5, are compared over the interval 200-1000 cm^{-1}.

The presence of the Raman mode centered at about 260 cm^{-1}, otherwise an inactive mode in oxide structures with the O_h symmetry, reflects a distortion of the orthorhombic structure. The suppression of this mode in the Co/Nb- codoped samples indicates a relaxation of the distortion of oxygen octahedra by the structural transformation of the orthorhombic $A2_1am$ phase to the lower symmetry $B2cb$ phase, which is in agreement with the XRD study.

The comparison of the Raman shifts and spectral intensities of the torsional and stretching modes from the BO_6 octahedra of the Co-free BiG1 sample and the Co-doped (BiG2, BiG3) samples indicates converse trends in compositional behaviour of the phonon modes at ~725 cm^{-1} and ~850 cm^{-1}. Upon doping, the Raman intensity of the former mode increases and the vibrational frequency of the CoO_6 octahedron shifts to higher wavenumbers, whereas the stretching mode of the oxygen octahedra remains centered around 850 cm^{-1} regardless of the Co content. Moreover, the spectral intensity of the 850 cm^{-1} phonon mode decreases as the Co concentration increases. This behaviour indicates that the introduction of the Co atoms into the bismuth-layered Aurivillius structure alters the local structural environment around the BO_6 octahedra in the mixed-layer samples. The evolution of the high-frequency Raman modes well correlates with the structural changes observed by XRD (Table S1), where the co-doping strategy resulted in the substantial anisotropy of the bond angles of the B-O-B chains in the outer octahedra (near the Bi_2O_2-fluorite type layer).

The spectral changes observed in the doped samples below 200 cm^{-1} are thought to be brought by different strain states in the mixed-layer structure, if compared to the parent four-layered $A2_1am$ phase. The soft Raman modes between 70 and 170 cm^{-1} are, according to the earlier theoretical and experimental studies [43,44], external modes closely associated with the A-site vibrations produced in the orthorhombic ABO_3 perovskite by the relative motion of the A cations against the slightly distorted oxygen BO_6 octahedra. In our earlier study of Raman spectra of Gd-doped BFTO [18], it has been shown that the characteristic triplet peak originating from the Raman active lattice modes of pure BFTO at around 93, 121, and 151 cm^{-1} is substantially suppressed and shifted to lower frequencies upon Gd doping. The damping effect was attributed to the reduced degree of Bi-O hybridization in perovskite-type slabs of the Aurivillius phase due to the dilution of bismuth lone pairs by gadolinium ions. From Fig. 4, one can see that the suppressed triplet mode of BiG1 re-appears in the doped samples with the most prominent peak at ~77 cm^{-1} and two small spectral features at about 123 and 151 cm^{-1}. It should be mentioned that the position and intensity of these peaks are not sensitive to the amount of the Co and Nb ions added. According to the work by Sun *et al.* [32], it can be suggested that different strain states in the three- and four- layered phases influence the vibrations of the Bi^{3+}

and Gd^{3+} ions at the A-sites of *B2cb* and *A2$_1$am* structures differently, leading to the observed changes in the low-frequency Raman spectra of our doped samples. The best resolved low wavelength feature near 50 cm^{-1} can be ascribed to a rigid-body mode and reflects the vibrations of the Bi^{3+} ion in the fluorite-type $(Bi_2O_2)^{2-}$ layer [44]. The small variation in the frequency of this mode is a consequence of the effective change in mass of the perovskite-like layers in the mixed-layered samples.

Mössbauer spectra analysis

The fitted ^{57}Fe Mössbauer spectra of the BiG1, BiG3 and BiG5 samples, as collected in transmission mode at 300 K are shown as solid circles in Fig. 5. The best fit to the data of the Co-free sample is obtained by using two quadrupole split doublets D(1) and D(2) with the isomer shifts IS(1)=0.35 mm/s and IS(2)=0.25 mm/s, and the quadrupole splitting parameters QS(1)=0.50 mm/s and QS(2)=0.72 mm/s, respectively. The presence of these two paramagnetic components with similar hyperfine interactions parameters evidences the existence of two non-equivalent sites for Fe ions in the Aurivillius *A2$_1$am* phase.
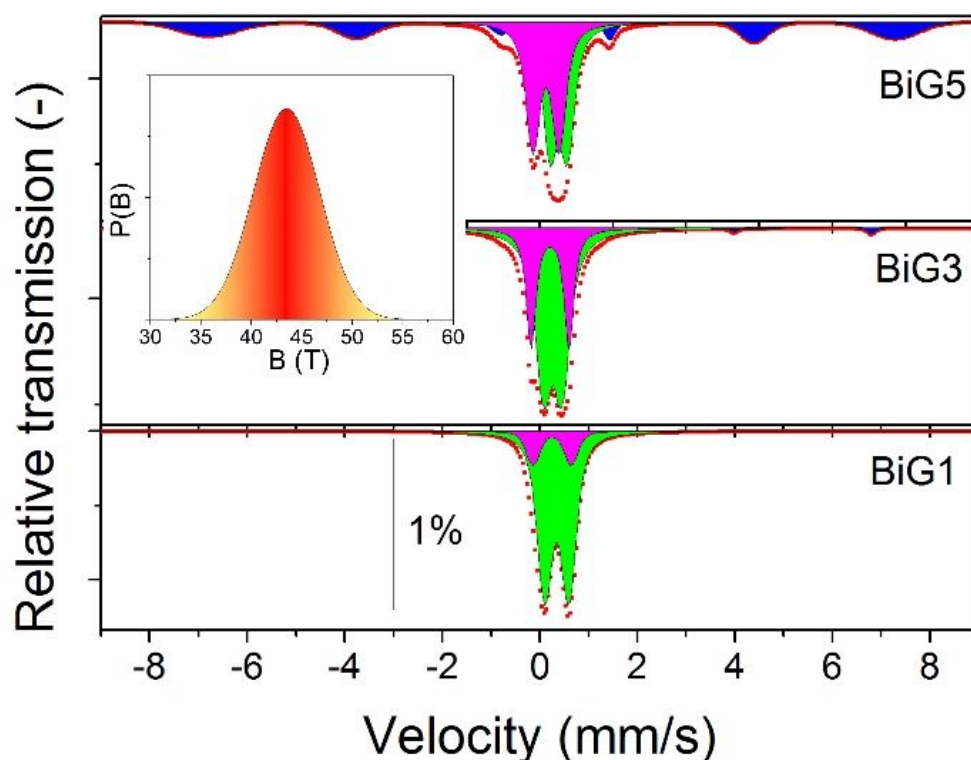

Figure 5. Fitted room-temperature Mössbauer spectra of BiG1, BiG3 and BiG5 (full red circles – total fit, pink and green doublets – paramagnetic contributions, blue sextet – hyperfine splitting). The inset illustrates the distribution of the hyperfine magnetic field induction for the BiG5 sample.

The obtained values of IS and QS are typical of the Fe^{3+} ion in an octahedral environment.[45] Because the size of the quadrupole splitting is closely related to the site distortion, the difference in the QS(1) and QS(2) values (~0.5 *vs.* ~0.7) suggests that the Fe^{3+} ions at the two octahedral sites experience different degrees of distortion. Given that the configuration of Fe^{3+} ions by six oxygen ions over the outer B(2) sites of the perovskite-like layer (adjacent to the fluorite-like $(Bi_2O_2)^{2+}$ layer) is less symmetrical than that over the inner B(1) sites, one can explain the larger value of the quadrupole splitting of Fe^{3+} ion occupying the outer B site, QS(2), if compared to that of Fe^{3+} ion in the inner B site, QS(1), by a higher electric field gradient. The similarity in the isomer shifts of both B(1) and B(2) sites is justified because the nearest surrounding of ^{57}Fe nuclei is practically the same (Fe^{3+} ions at B(1) and B(2) sites are surrounded by six oxygen ions in the first coordination sphere and eight bismuth ions in the second sphere). Similar findings about the Fe^{3+} ion characteristic in bismuth-layered Aurivillius-phase materials were reported on the basis of Mössbauer analysis by Lomanova *et al.* [46] and Jartych's group [11,20].

In Fig. 5, the Mössbauer spectra of the doped samples BiG3 and BiG5 show the presence of a sextet in addition to two doublets. While the paramagnetic contribution can be attributed to the $Bi_{4.3}Gd_{0.7}FeTi_3O_{15}$ phase, which shows no magnetic ordering at room temperature, the sextet indicates that part of the B-site cations (Fe^{3+} and Co^{3+}) are magnetically ordered. The presence of both doublet and sextet in the Mössbauer spectra is apparently associated with the irregular mixed-layering of the three- and four- layered perovskite slabs.

Besides providing the IS and QS values, the numerical fitting of the Mössbauer spectra allowed determining the hyperfine magnetic field (H_{hf}) and its distribution. For BiG5, the fitted values of the isomer shift and the quadrupole shift of the sextet are 0.29 mm/s and -0.04 mm/s, respectively. The effective value of the hyperfine magnetic field induction ($B_{eff} = \mu_0 H_{hf}$, where μ_0 is the magnetic permeability of vacuum) was found to be about 43.5 T, which is in agreement with the values reported for multi-layered Aurivillius materials exhibiting multiferroic properties [29]. The obtained B_{eff} distribution is presented in the inset of Fig. 5 and its broadness reflects a random occupation of B sites by $Fe^{3+}/Co^{3+}/Ti^{4+}/Nb^{5+}$ ions in the oxygen octahedra of the perovskite-like layers. All the hyperfine interactions parameters for the Co-free (BiG1) and Co-doped (BiG3 and BiG5) samples are summarized in Table S3.

3.3 Magnetic properties and electronic structure

19

SQUID and VSM magnetometry

Figs. 6(a) and 6(b) show the magnetic field dependence of the magnetization (M-H) of the Co-free (BiG1), Co-doped (BiG2 and BiG3), and Co/Nb- codoped (BiG4 and BiG5) samples, as obtained at 300 K and 5 K, respectively. While the M-H plots of the Co-free Aurivillius compounds demonstrate a pure paramagnetic behaviour (a linear field-dependence of magnetization) with no noticeable hysteresis or remanent magnetization at both temperatures, the magnetization hysteresis loops of the doped samples obtained at 300 K indicate the presence of the long-range magnetic order. Due to the paramagnetic contribution of the four-layered phase in the mixed-layer BiG2-BiG5 samples, saturation of the magnetization was not reached in the entire temperature range 5-350 K even under the maximum applied field of $\pm$ 5 T. As shown in the insets of Fig. 6(a) and 6(b), the introduction of a small amount of the Co^{3+} ions gives rise to the appearance of the spontaneous magnetization; however, the magnetization decreased when the amount of the Co added was increased to the level of the Fe concentration.
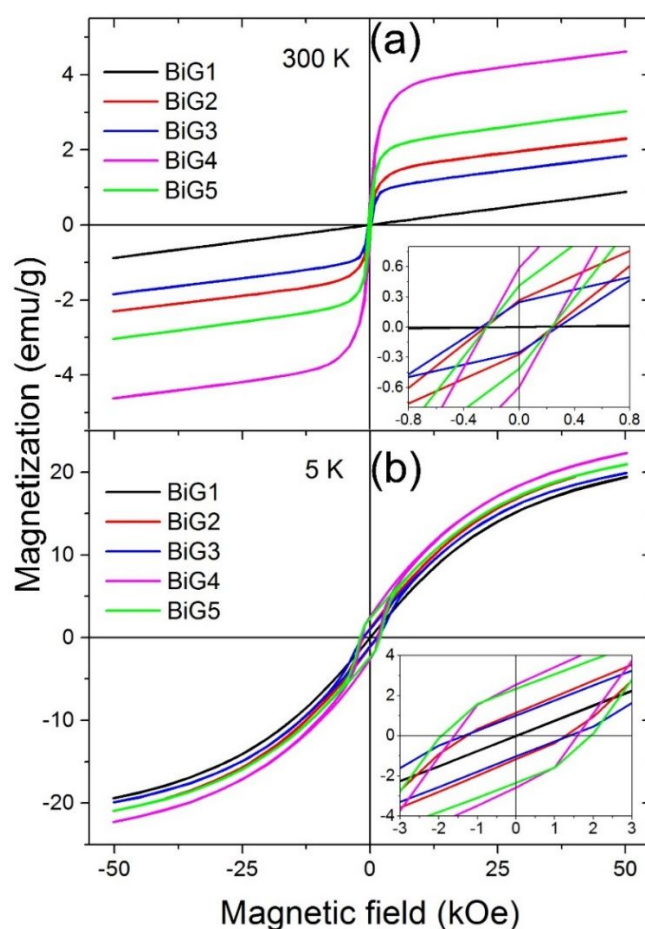

Figure 6. Field dependence of the magnetization of the BiG1-BiG5 samples, as recorded at (a) 300 K, and (b) 5 K. The insets show the enlarged sections of the M-H hysteresis loops within the selected low magnetic field region.

20

Zhang *et al.* [29] have investigated the magnetic properties of structurally similar rare-earth-doped four-layered Aurivillius compounds in the entire concentration range of Co (x=0-1) and found that the remanent and saturation magnetizations of $Bi_4NdTi_3Fe_{1-x}Co_xO_{15}$ reached a maximum at x=0.3. In the rare-earth-free $Bi_5Fe_{1-x}Co_xTi_3O_{15}$ (BFCT) series, the maximum magnetization has been reported at x=0.5.[47] For x>0.6, the BFCT samples exhibited mostly paramagnetic characteristics. In our study, for x=0.5, the coercive field (H_c) of BiG3 is about 275 Oe and 1258 Oe at 300 K and 5 K, respectively. The room-temperature remanent magnetization ($2M_r$) is about 0.50 emu/g, which is almost three times bigger than the value reported for $Bi_4NdFe_{0.5}Co_{0.5}Ti_3O_{15}$ in Ref. 29 ($2M_r$~0.17 emu/g), and about two orders of magnitude larger than that of BFCT at room temperature ($2M_r$~7.8 memu/g) [47]. The co-substitution with Nb^{5+} ions brings along an enhancement of the magnetization and lowering the magnetic coercivity, making the BiG4 sample with the stoichiometric composition of $(Bi_{4.3}Gd_{0.7})(Fe_{0.7}Co_{0.3})_{1.3}Ti_{2.4}Nb_{0.3}O_{15}$ the magnetic material with the largest saturation magnetization (M_s~3.7 emu/g, determined from Fig. 6 by extrapolation to the *y*-axis) and the biggest value of the remanent magnetizations ($2M_r$~1.2 emu/g) at room temperature, if compared to the values of other doped samples. The remanent magnetization of BiG4 is more than twice the value of the Co-doped samples (BiG2 and BiG3) and exceeds by far the largest $2M_r$ value (~0.8 emu/g) reported for the four-layered rare-earth (La, Nd, Ho)- substituted BFCT ceramics [26].

Upon cooling, both $2M_r$ and $2H_c$ of all the doped samples under investigation continuously increase; however, the former exhibits a plateau at temperatures below 150 K (see the insets of Fig. S3). The monotonic increase of the coercive field with decreasing temperature is a characteristic feature of a ferromagnet and reflects a gradual increase in the anisotropy and/or magnetoelastic energy. The representative M-H plots for the BiG3 and BiG5 samples, as obtained at several different temperatures within the temperature range of 50-350 K, are shown in Supplementary material in Figs. S4(a) and S4(b), respectively. The low-temperature magnetic behaviour of the Aurivillius-phase materials will be discussed in detail in the context of thermomagnetic ZFC/FC measurements in the following section.

From the VSM magnetization data recorded at a magnetic field of 1000 Oe in the temperature range from 300 K to 720 K (Fig. 7), it appears that the sample with the lower concentration of Co (BiG2) undergoes a magnetic transition to a paramagnetic state at much higher temperature (T_{cm}~623 K; defined as the temperature corresponding to the peak of the

21

differential dM/dT, as shown in the inset of Fig. 7) than BiG3 (T_{cm}~403 K). The transition temperature T_{cm} of the BiG3 sample is in the range of the paramagnetic Curie temperatures obtained by fitting the Curie-Weiss behaviour of $Bi_{4.2}Nd_{0.8}Ti_3Fe_{0.5}Co_{0.5}O_{15}$ (T_{cm}~420 K) [26] and $Bi_{4.25}Gd_{0.75}Ti_3Fe_{0.5}Co_{0.5}O_{15}$ (T_{cm}~370 K) [28]. Moreover, the additional Nb doping shifts further the transition temperatures far from room temperature, resulting in the loss of long-range magnetic order in the BiG4 and BiG5 samples at about 698 K and 443 K, respectively. The right shift of T_{cm} along with the higher magnetic moment of BiG4 and BiG5 can be attributed to the increased content of magnetic cations (Fe^{3+}, Co^{3+}) in the perovskite-like layers of the mixed-layer Aurivillius structures by the replacement of Ti^{4+} at B sites with the donor Nb^{5+} ions. The Nb-substitution-induced enhancement of the magnetic state of BFCT is in accordance with the results of Mössbauer spectroscopy (see Fig. 5 and Table S3), where the effective hyperfine magnetic field of BiG3 was found to increase from 40.3 T to 43.7 T (BiG5) on Nb doping. The T_{cm} values for $CoFe_2O_4$ and $FeCo_2O_4$ were reported around 720.5 K [48] and 460 K [49], which are far away from the observed magnetic transitions. Thus, these spinel-type impurities, although magnetic in nature [50,51], are unlikely to be the main contributors to the measured magnetization above room temperature.
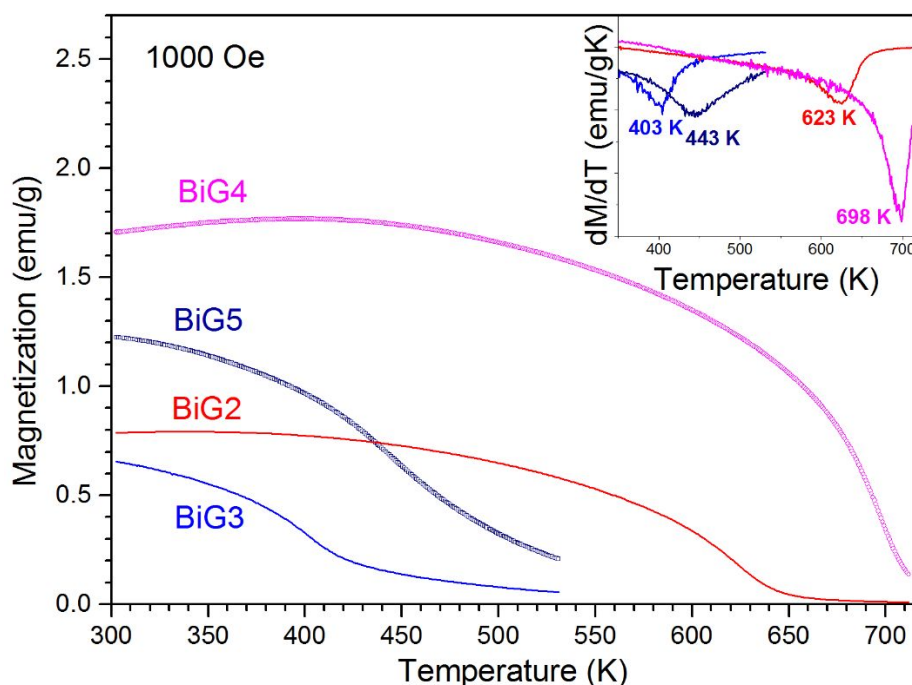

Figure 7. Temperature dependence of the magnetization of the BiG1-BiG5 samples, as collected at a magnetic field of 1000 Oe (the inset shows the magnetic transition temperatures of the respective samples).

According to our earlier theoretical and experimental studies [8,22], at least two main intrinsic contributions should account for the observed magnetization in the Co-doped BFTO samples: (i) Fe^{3+}-O-Co^{3+} or Fe^{3+}-O-Co^{2+} exchange interaction in iron-rich areas, and (ii) spin canting via antisymmetric DMI. In the three-layered $Bi_{3.25}La_{0.75}Ti_{2.5}Nb_{0.25}(Fe_{0.5}Co_{0.5})_{0.25}O_{12}$ single-phase Aurivillius ceramics with the orthorhombic $B2cb$ structure, the weak ferromagnetism was suggested to originate from the local Fe/Co rich regions, in which superexchange interactions between adjacent Fe and Co ions through an oxygen atom are responsible for the long-range magnetic order. In line with the Goodenough-Kanamuri rule [52], superexchange interactions between the neighboring Fe d half-filled orbital and the Co d empty or fully-filled orbital can give rise to the ferromagnetic coupling in the BFCT Aurivillius-phase materials. Such ferromagnetic coupling may lead to a locally-ordered magnetic structure and macroscopic (observable) magnetization. However, this mechanism does not explain satisfactorily the limited concentration of Co ($x \approx 0.3$) at which the remanent and saturation magnetizations of our samples exhibit their maxima. Obviously, the appearance and enhancement of the magnetization cannot be attributed to the magnetic moment of the Co^{3+} ion, which is smaller ($\sim 4.9\ \mu_B$) than that of the Fe^{3+} ion ($\sim 5.3\ \mu_B$). Zhang $et\ al.$ [53] have proposed that the occurrence and gradual enhancement of the magnetization in iron-rich areas of the Co-doped BFTO-derived compounds is mainly contributed by the population of Fe^{3+}-O-Co^{3+} local structures.

Another possible contribution to the observed magnetization of the doped (BiG2-BiG5) samples can be linked with the structure evolution and changes of the B-O-B bond angles in perovskite-like slabs. In rare-earth-doped $BiFeO_3$, the substitution-induced structural changes were found to bring about the ferromagnetic order in the canted G-type antiferromagnetic structure via the indirect antisymmetric exchange due to the substitution-enhanced canting of Fe^{3+} spins.[54] Similar compositional effects are thought to occur in the phase-modulated samples (BiG2-BiG5) because of the complicated internal strain distribution over the mixed-layer structure and substitution-induced tilting distortion nearby special interfaces of the two different perovskite slabs. In the Co doped samples, spin canting of both the Fe- and Co-based sublattices, caused by tilting of the adjacent FeO_6 and CoO_6 octahedra, can give rise to the observed magnetization through the DMI. The additional Nb substitution makes the oxygen octahedra more distorted (see Table S2; the bond angles of B-O-B chains along the c-axis in the inner perovskite-type layers decrease from 160.6^0 in the $A2_1am$ phase to 158^0 in the $B2cb$ phase and correspondingly in the outer layers from 162^0 to 158^0) with slightly increased octahedral tilting, facilitating the alignment of the Fe and Co spins along the magnetic field.

The improved spin orientation results in the enhanced magnetization of the Co/Nb- codoped samples (BiG4 and BiG5), if compared to the resulting magnetic moment of the Co-doped samples (BiG2 and BiG3).

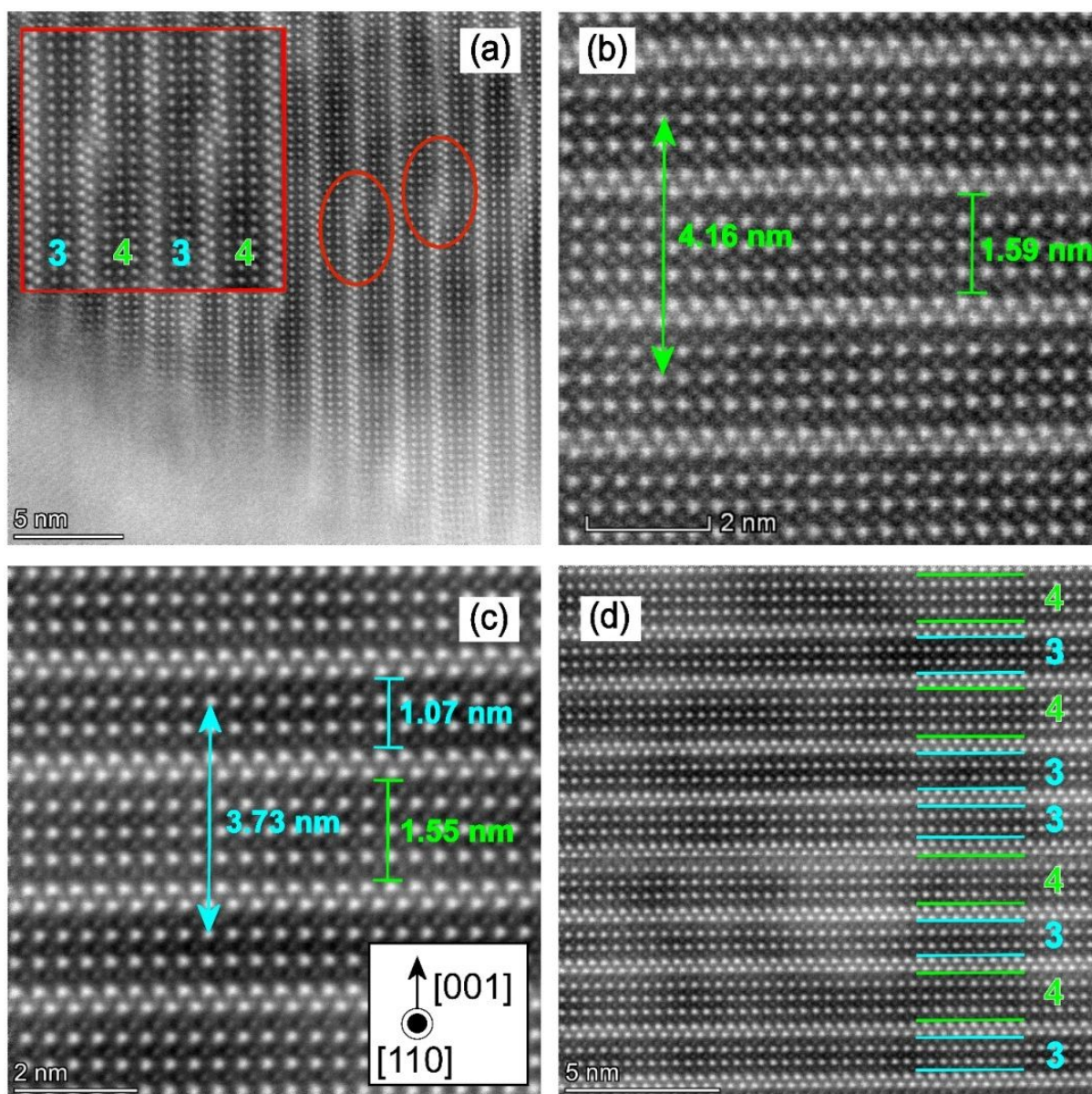*High resolution TEM imaging and nanoscale structural modulation*

Figure 8. STEM-HAADF images of (a) BiG3, (b) BiG1, and (c, d) BiG5. The orderly arranged bright spots represent bismuth atoms; the inset and red open ellipses in (a) confine the defect area in the mixed-layer structure, where the nanoscale structural modulation appears. The thicknesses of the pseudo-perovskite slabs in three- and four-layered phases is highlighted in (b) and (c). The disordered intergrowth of the two phases in the BiG5 sample is illustrated in (d).

The decrease in the magnetic moment of the BiG3 and BiG5 samples is thought to be related to the AMT boundary, which is an intrinsic characteristic of mixed-layer Aurivillius-type structures.[32] The results of our XRD and Raman spectroscopy studies revealed the composition-driven structural evolution in the BiG2-BiG5 samples with the coexistence of the four- and three- layered phases. Accordingly, we propose that the ferromagnetic Fe-O-Co clustering in the mixed-layer samples is driven by the NSM, which is generated inside the two-phase Aurivillius structure and affects both the superexchange interaction between magnetic (Fe, Co) ions and spin canting, in particular, at the interface of the two phases. The driving force for these defects and their further population is not clear but could be linked with a strain gradient at grain boundaries and the presence of secondary phase impurities, such as sillenite-type $Bi_{12}TiO_{20}$ and Fe-rich and/or Co-rich spinels. Indeed, a majority of the slipped Bi_2O_2 layers (a kind of the Frenkel defect, where Bi ion is shifted from its lattice point) are observed in those regions of the Aurivillius-phase grain, which are close to the neighbouring grain or impurity (see Fig. 8(a)). The NSM accompanied by a large strain mismatch could give rise to the short-range ordered Fe-O-Co polar clusters in the host lattice at the interface of the three- and four-layered phases. Figs. 8(b), and 8(c)-(d) show the representative atomic resolution HAADF images, taken using an aberration-corrected scanning transmission electron microscope (S-TEM) of the four-layered phase of BiG1 and the mixed-layer BiG5 sample, respectively.

It has been demonstrated that the Fe and Co ions tend to occupy the same perovskite slabs and are distributed randomly within both four and three perovskite-like layers. [30-32] That means that the Fe- or Co- occupied octahedra may distribute in a disordered fashion inside the perovskite slabs (see the illustration in Fig. S4(a) and S4(b)) and for some of CoO_6 octahedra there is great possibility to be adjacent to FeO_6 octahedra at the interface between the two phases (Fig. S4(c)), increasing the possibility of Fe-O-Co coupling and the formation of the ferromagnetic state (Fig. S4(d)). In addition, the structural distortion in perovskite-like slabs upon the Co substitution is more pronounced when some Ti ions at B sites are partially replaced by Nb ions. The enhanced ferromagnetic-type clustering is believed to be responsible for the high magnetization of BiG4, as shown in Fig. 7.

The cobalt doping level $0.3 \leq x \leq 0.5$ appears to correspond to the AMT boundary across which the four-layered phase (Fig 8(b)) transforms to the three-layered phase (Fig. 8(c)). This layer-number reduction is accompanied by the structural phase transformation from $A2_1am$ to $B2cb$. In the x=0.5 samples (BiG3 and BiG5), the calculated fraction of the $B2cb$ phase was found to be higher than that in BiG2 and BiG4 (x=0.3). In addition, the introduction of Nb ions

25

resulted in the dominance of the *B2cb* phase in the Aurivillius structures BiG4 and BiG5. It is anticipated that above the AMT boundary ($x \geq 0.5$) the phase-modulated structure with disordered intergrowths of four- and three- layered perovskite slabs (the structurally disordered system) will turn into the ordered (almost NSM-free) structure with more homogeneous distribution of Co ions. Due to a larger strain mismatch between the outer perovskite-like layer and Bi_2O_2 layer in the three-layered phase, if compared to that in the four-layered phase, the increased content of Co ions (above the AMT) accompanied by the higher amount of the three-layer *B2cb* phase may also result in an increased occupation of the Co^{3+} ions in the outer perovskite units [30], so reducing the spin canting effects and, ultimately, weakening the ferromagnetism.

Apart from the superexchange interaction between the Co^{3+} and Fe^{3+} ions through oxygen ions, a double exchange between a mixed valence iron (Fe^{3+}/Fe^{2+}) or cobalt (Co^{3+}/Co^{2+}) through oxygen may result in the ferromagnetic order, too. The valence fluctuation of the Fe and Co ions has been reported to exist in Aurivillius-type oxides.[32,53]. Zhang *et al.* [53] have demonstrated oxygen-vacancies induced ferromagnetism in the four-layered $Bi_4NdTi_3FeO_{15}$ multiferroic ceramics. On the other hand, Zuo *et al.* [55] have investigated the effect of Nb ions on the valence state of Fe and Co ions in $Bi_5FeTi_2Nb_{0.5}Co_{0.5}O_{15}$ ceramics using X-ray photoelectron spectroscopy and found that the donor doping reduces the number of oxygen vacancies, leading to the enhanced ferromagnetic state.

Synchrotron X-ray Absorption Spectroscopy (XANES Fe- and Co- K edge spectra)

In order to determine the valence state of Fe and Co ions and investigate the degree of Fe-O and Co-O hybridization upon Co-doping and Co/Nb- codoping, we performed X-ray absorption spectroscopy at the Fe and Co *K*-edge for all the samples. On the basis of the group theory, it has been demonstrated that the synchrotron X-ray absorption at metal *K*-edge is accompanied by the excitation of a $1s$ electron to valence bound states localized on the metal ion.[56] In case of $3d$ transition metals such as Fe and Co (in which the valence electrons reside in p orbitals), the *K*-edge spectra are primarily contributed from the $1s \rightarrow 4p$ dipole transition, but there are also contributions from weak dipole-forbidden $1s$-to-$3d$ excitations involving transitions to the $2t_{2g}$ and $3e_g$ Fe d orbitals [54]. These electronic transitions are partially allowed because of the electric quadrupole coupling and/or $3d$-$4p$ orbital mixing. Since the mixing of metal $4p$ orbitals with the $3d$ orbitals depends strongly on the coordination symmetry, the *K*-edge spectral features are sensitive to the coordination number, number of d-electrons and the octahedral environment. Therefore, the Fe and Co *K*-edge XANES spectra of the samples in

$(Bi_{4.3}Gd_{0.7})(Fe_{01-x}Co_x)_{1+y}Ti_{3-2y}Nb_yO_{15}$ series are expected to be different when the chemical bonding environment of B-O-B chains in the perovskite slabs changes on doping.
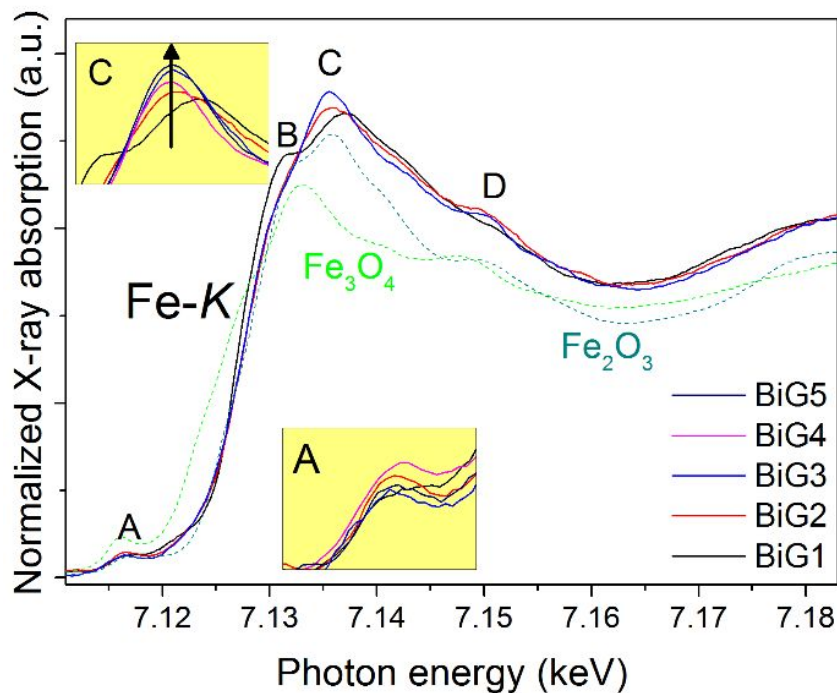

Figure 9. XANES Fe K-edge spectra of the BiG1-BiG5 samples and reference powders of hematite (α-Fe$_2$O$_3$) and magnetite (Fe$_3$O$_4$), as collected at room temperature. The insets show a zoomed part of spectral peaks A and C.

Fig. 9 shows the normalized Fe K-edge XANES spectra of BiG1-BiG5 samples and reference oxides (α-Fe$_2$O$_3$ and Fe$_3$O$_4$). The energy is calibrated by a standard Fe metal foil with a threshold edge energy of E_0=7112 eV. From the figure, one can distinguish two characteristic regions in the spectra: (i) the pre-edge region involving a small peak (the A peak) at about 7117 eV contributed from the one-electron $1s \rightarrow 3d$ transitions, and (ii) the rising edge region, which comprises of several notable spectral features (denoted here and after as the peaks B, C and D). The energy position of the raising edge (determined from the maximum of the first-derivative spectrum) is about 7128 eV for all the samples under investigation and corresponds to the $1s$-$4p$ transition. Generally, the raising edge is used as an indicator of the oxidation state of an element assuming a similar ligand environment.[56] When the oxidation state rises, there is a shifting of the absorption edge towards higher energies. In addition, higher oxidation of the metal leads to greater stabilization of the $1s$ orbital with respect to the metal $3d$ orbitals, thus, leading to higher energy of the pre-edge feature. In the present data, no shift in the rising edge

position and neither in the pre-edge peak position is observed, which rules out the valence fluctuation of iron going from the Co-free BiG1 sample to the Co/Nb- codoped (BiG2-BiG5) samples through the Co-substituted BiG2 and BiG3. The spectral profile and the rising edge position of all the samples are similar to these of the α-Fe_2O_3 standard, confirming the trivalent state of Fe ions in the parent Gd-substituted Co-free BFTO [18], as well as in the Co-doped compositions. Hence, one can infer that the partial replacement of Fe ions by Co ions does not cause valence change of iron in the mixed-layer Aurivillius materials. Furthermore, the spectral similarity of the Aurivillius samples and hematite implies that the Fe^{3+} ions in perovskite-like layers are octahedrally coordinated to their six nearest-neighbor oxygen atoms; four in the basal plane and one each above and below. The Co substitution, however, does change the pre-edge intensity across the series, as shown in the inset A of Fig. 9. As the small amount of cobalt is introduced (x=0.3) the pre-edge peak slightly increases. The increase in the number of electric dipole-forbidden 1s-to-3d transitions is further accentuated by Nb doping and can be associated with an increase in the number of holes in the 3d shell as well as an increase in covalently mediated 3d-4p mixing. Jiang et $al.$ [57] proposed that in TiO_6 octahedra the higher mixing of the 4p with the 3d orbitals arises from a reduction in the Ti-O bond length. In the present study, the XRD results showed that the Co/Nb- codoping causes the reduced B-O bond anisotropy by decreasing some B-O bond lengths in the octahedron cage.

With the increased doping level of Co from x=0.3 to x=0.5, the spectral intensity of the pre-edge peak of BiG3 was found to decrease down to its original value (BiG1), which further justifies the results of the magnetic-property measurements (i.e., the reduced magnetization) by an increased number of 3d electrons [58]. An opposite trend is observed in the post-edge feature (peak C), which natively signifies the dipole-allowed transitions to unoccupied 4p states. Thus, the increasing of the Co content up to the AMT boundary (0.3≤x<0.5) promotes the inclusion of Fe 4p characters into Fe 3d orbitals, thereby enhancing the electric dipole transition of a 1s electron to a p-d hybridized orbital. Further doping results in a substantial increase of the 1s-4p dipole-allowed transitions, while decreasing the intensity of the pre-edge A peak due to the suppression of the 3d-4p orbital mixing. Using the DFT simulations Wen et $al.$ [59] have shown that variations of the rising edge features (intensities of the B and C peaks) in the Fe K-edge XANES spectrum of $BiFeO_3$ are directly related to changes in the octahedral tilt. They ascribed a decrease of absorption at the energy corresponding to the peak C to a reduction of tilting distortion. Accordingly, we can associate the observed increasing of the C peak in the Fe K-edge XANES spectra of BiG4 and BiG5 samples with the substitution-induced increase in octahedral tilting (see Tab. S2).

A shoulder peak (feature B) located on the rising K-edge of the Aurivillius-phase samples is likely caused by the shakedown process or the so called the ligand-to-metal charge transfer process [56]. It is more evident for BiG1 and reflects a formally forbidden two electron $1s\rightarrow4p$ transition that leads to relaxation of the excited state, followed by a ligand-to-metal charge transfer to the excited state. The diminishing of this peak in ferrite perovskites is usually associated with changes in local symmetry of the Fe structure. Spectral feature D results from the multiple-scattering contribution of absorbing Fe in FeO_6 octahedra surrounded by Bi and Gd ions.

The Co K-edge XANES spectra of the Co-substituted samples (Fig S6(a)) appear, at first sight, similar to those recorded at the Fe K-edge, implying that the local structure surrounding the Co atoms is similar to that of Fe atoms. Though, the pre-edge structures (peak A) from the quadruple $1s$-$3d$ transitions into unoccupied t_{2g} and e_g minority states at about 7715 eV are notably weaker than those at Fe K-edge and the spectral intensity of the peak C decreases upon doping, suggesting a suppression of the dipole-allowed $1s$-$4p$ transitions accompanied by the increased degree of the $3d$-$4p$ orbital mixing due to the Co substitution induced changes in local structure. The rising edge position of all the doped samples is about 7725 eV (peak B) and corresponds to the edge energy of the Co_3O_4 standard (Fig. S5(a)), known as a mixed valence compound, containing both Co^{2+} and Co^{3+} oxidation states. The energy difference between the rising edges of the two features B and C in Fig. S5(a) is about 3.4 eV, which is close to the difference of 3.1 eV between CoO (Co^{2+}) and Co_2O_3 (Co^{3+}) [60]. The radial distribution functions for the BiG2-BiG5 samples, as obtained by Fourier transform (FT) of the EXAFS function, $\chi(k)$, into real space, are shown in Fig. S5(b) and reveal a set of four distinct peaks in the range of 0–5.5 Å corresponding to interatomic distances of the Co-O, Co-Bi/Gd, Co-Co, and Co-O-Co/Fe bonds. From the figure, one can see that while the first-shell Co-O bond lengths and Co-O-Co/Fe chains in the fourth coordination sphere are reduced, the distance between the Co and A-site ions in the second shell and the third-nearest-neighbor distance of cobalt atoms (Co-Co) do not change upon the Co substitution. It should be noted that the partial replacement of Ti^{4+} ions by Nb^{5+} ions has an opposite effect on the Co-O bonds and leads to their elongation. Furthermore, the Co-substitution and Co/Nb- codoping substantially affect the FT magnitude of the EXAFS function below 3.7 Å. With x increasing from 0.3 (BiG2) to 0.5 (BiG3, above the AMT), the peak corresponding to the Co-O bond shows a huge increase in the intensity, resulting in the increased relative intensity ratio of the Co-O peak to the Co-Bi/Gd peak. Surprisingly, the introduction of Nb ions into the x=0.3 samples has the opposite effect and causes an abrupt increase of the Co-Bi/Gd peak in the BiG4 sample, making the relative

intensity ratio of the two peaks strongly reduced. Considering the results of VSM and SQUID magnetometry, it is proposed that the Co substitution-induced enhancement of magnetization can be related to the strengthening Co-Bi/Gd bonds and increasing the Co-O bond lengths accompanied by the elongated Co-O-Co/Fe chains.

Thus, the XANES results are consistent with the previous finding that the Co and Co/Nb doping affects the octahedral tilting and changes the chemical bonding environment of B-O-B chains in the perovskite slabs of the Aurivillius materials. These substitution-induced structural changes, accompanied by variations in the electronic structure, influence the macroscopic properties such as the observed magnetization. Combining the results of the XANES spectra analysis and first principles DFT calculations, Lee *at al*. [61] have shown that the degree of the 3d-4p orbital mixing in ferrite perovskites can be directly linked with density of states in the Fe orbitals (d, p). They revealed that upon La doping the number of occupied stated in the Fe d orbital increases, giving rise to the enhanced magnetization due to the reduced degree of the 3d-4p orbital mixing. Similar findings on improving the magnetization of $BiFeO_3$-derived multiferroics by the A-site rare earth (Tb) substitution have been reported in our earlier work, too.[54] The enhanced magnetic moment, contributed by the increased spin canting via the antisymmetric DMI, was attributed to the increase in the number of the occupied 3d states reflected by the suppression of the Fe K pre-edge XANES feature. In the present Aurivillius-phase oxides, the NSM occurs at the interface of the three- and four- layered phases upon the Co substitution and Co/Nb- codoping, producing possible local short-range ordered and elongated Fe-O-Co polar clusters. The ferromagnetic-type clustering is limited by the AMT boundary (0.3≤x≤0.5), i.e., the Co doping level which controls the density and distribution of the Bi_2O_2 shifts. For the half cobalt substituted samples (BiG3 and BiG5), the strain mismatch of the two phases is thought to be reduced by the growing of the three-layered $B2cb$ structure, which becomes the prevailing phase in the Co/Nb- codoped sample.

Considering the dominant role of the ferromagnetic clustering in the observed macroscopic magnetization, one can correlate the reduced magnetization of the x=0.5 samples (BiG3 and BiG5) with the increased tilting distortion accompanied by the increased degree of the Fe 3d-4p orbital mixing and the decrease in the number of occupied states in the Fe d orbital [61]. Thus, the strengthening of the Fe 3d-4p hybridization in the samples with the excessive Co doping level (x≥0.5, above the AMT boundary) can be accounted, at least partly, for the shortening of the B-O-B chains, and subsequently for the suppression of the Fe-O-Co clustering in the Aurivillius materials under investigation.

ZFC and FC magnetizations and SG-like behaviour

For a better understanding of the magnetic interactions in the doped Aurivillius-phase samples with the phase-modulated structure, the temperature dependence of magnetization in zero-field cooled (ZFC) and field-cooled (FC) modes was carefully examined in the temperature range 5-300 K. The ZFC-FC thermomagnetic curves for the BiG1-BiG5 samples subjected to an external DC magnetic field of 100 Oe and 1000 Oe are shown in Fig. S6 and Fig. 10a, respectively. While the Co-free BiG1 (x=0) sample exhibits conventional paramagnetic behaviour with reversible ZFC-FC magnetization curves, the ZFC-FC curves of the doped samples bifurcate and show a thermo-magnetic anomaly (a broad peak) at temperatures below the T_{cm} (for the ferromagnetic transition temperatures, T_{cm}, see the inset of Fig. 7). This behaviour roughly indicates the magnetic frustration and glassy behaviour of the mixed-layer samples at low temperatures. Random spin freezing is thought to be brought about by a competition between (weak-) ferromagnetic and antiferromagnetic interactions occurring in the structure of local short-range ordered Fe-O-Co clusters embedded in the paramagnetic host lattice with antiferromagnetic ordered Fe and Co ions at very low temperatures. The peak of the ZFC magnetization centered at about $T_f \approx 250$ K is more evident for the samples with lower T_{cm} (BiG3 and BiG5) and under a high DC magnetic field of 1000 Oe (above H_c).
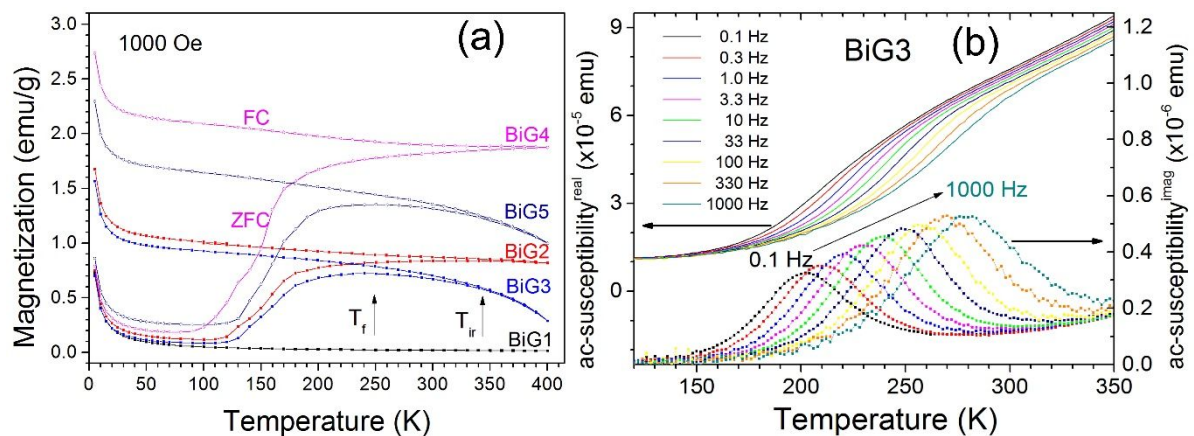

Figure 10. Spin glass-like behavior of the phase-modulated Aurivillius samples at low temperatures. (a) Temperature dependence of the ZFC and FC magnetization of BiG1-BiG5, as measured at a field of 1000 Oe. (b) AC susceptibility of the BiG3 sample in the temperature interval of 120-350 K; the in-phase (real) and out-of-phase (imaginary) components of the susceptibility were collected at nine different frequencies between 0.1 Hz and 1000 Hz.

It should be noted that the characteristic temperature T_{ir} at which the thermo-magnetic irreversibility appears is clearly larger than T_f, and both temperatures shift towards lower temperatures with increasing H, similar to that usually observed in spin-glass (SG) materials. The field-driven shift of the T_f is a characteristic feature of ordinary spin glasses [62] and is consistent with the fact that higher magnetic field weakens the occurrence of a cluster spin-glass state, which in turn shifts the T_f towards lower temperature. Below T_f, the ZFC magnetization tends to fall rapidly. The sudden decrease in the magnetization can be attributed to spin glass behaviour of interacting Fe-O-Co clusters. Below 100 K, the magnetic Co and Fe ions are coupled into a spin frustrated state of low magnetization. From Fig. 10a, one can see that even at as high magnetic field as 1000 Oe the ZFC and FC curves of the BiG4 and BiG5 samples are heavily bifurcated at low temperature, which is an indicative of a strongly frozen spin state in these samples.

In order to confirm the SG-like effect in the mixed-layer structures, we performed an AC susceptibility measurement on BiG3, as a representative Aurivillius sample, in the frequency range of $0.1 \leq \omega/2\pi \leq 1000$ Hz. Fig. 10b shows the in-phase (real) $\chi'_{ac}(T, \omega)$ and the out-of-phase (imaginary) $\chi''_{ac}(T, \omega)$ component of the AC susceptibility measured as a function of temperature between 120 K and 350 K at nine different frequencies. When the temperature is decreased below T_{cm}, the in-phase component decreases monotonously, whereas χ''_{ac} exhibits a pronounced peak indicating the presence of a relaxation process. Indeed, from the figure, it is obvious that both χ'_{ac} and χ''_{ac} are frequency dependent in the temperature interval 150-350 K. Upon increasing ω the maximum of χ''_{ac} shifts to higher temperature, which is characteristic of spin glasses.[62] Further analysis of the AC susceptibility data revealed that, in the vicinity of the critical temperature, SG-like cooperative freezing obeys the critical slowing down dynamics (see Supplementary material).

From the analyses of the DC (ZFC/FC magnetization) and AC (complex susceptibility) thermomagnetic data, it can be inferred that the low-temperature SG-like state and relaxation behaviour of the doped samples (BiG2-BiG5) is brought by the cooperative, non-equilibrium, freezing of randomly distributed Fe-O-Co clusters. Similar features of the spin freezing have been observed, for instance, in highly disordered systems, as well as in site-ordered geometrically frustrated antiferromagnets.[63,64] The occurrence of the ferromagnetic (non-) homogeneous clusters in the Co-substituted Aurivillius-phase compounds is driven by the NSM and their contribution to the macroscopic magnetization is controlled by the AMT doping level.

4. Conclusions

In summary, the in-depth analysis of the phase evolution, structural changes and variations in the electronic structure of the $(Bi_{4.3}Gd_{0.7})(Fe_{01-x}Co_x)_{1+y}Ti_{3-2y}Nb_yO_{15}$ (x=0, 0.3 and 0.5; y=0 and 0.3) oxides was carried out to elucidate the room-temperature ferromagnetism and low-temperature spin glass-like behaviour of the Co-doped BFTO-derived Aurivillius compounds. It is demonstrated that both phenomena occurring in different temperature windows can be attributed to the phase-modulated structure of the doped system. By increasing the amount of the Co added, the four-layered $A2_1am$ parent phase gradually transforms to the thee-layered orthorhombic phase of a lower symmetry (space group $B2cb$) forming a mixed-layer structure where the two phase coexist. This substitution effect is further enhanced by the donor Nb doping, which results in the mixed-layer Aurivillius structure with the dominant three-layered phase. At the interface of the two orthorhombic phases, a nanoscale structural modulation accompanied by disordered intergrowth of these phases was observed. The substitution-induced changes in the crystal structure (lattice distortions, octahedral tilting) were found to affect the electronic structure of the intergrowths Aurivillius materials. Due to the reduced degree of the $3d$-$4p$ orbital mixing, the introduction of a small amount of Co is suggested to give rise to the appearance of magnetization by promoting the formation of possible local short-range ordered Fe-O-Co polar clusters nearby the interface of the four-layered and three-layered phases. This ferromagnetic-type clustering is controlled by the Aurivillius morphotropic boundary above which the magnetization of the mixed-layer structures decreases. The existence of the randomly distributed ferromagnetic clusters and their cooperative freezing is proposed to be responsible for the observed relaxation (SG-like behaviour) of the Co-doped BFTO-derived Aurivillius compounds at cryogenic temperatures.

ASSOCIATED CONTENT

Supporting information

The Supporting Information is available free of charge on the RSC Publications website at DOI:

AUTHOR INFORMATION

Corresponding Author

*E-mail: vkoval@saske.sk

33

ORCID

Vladimir Koval: 0000-0003-2425-8738

Radovan Bures: 0000-0003-0827-405X

Karel Saksl: 0000-0001-8133-5352

Pavla Roupcova: 0000-0002-3969-58378

Chenglong Jia: 0000-0003-2064-923X

Haixue Yan: 0000-0002-4563-110

Author Contributions

The manuscript was written through contributions of all authors. All authors have given approval to the final version of the manuscript.

Notes

The authors declare no competing financial interest.

REFERENCES

[1] N. A. Spaldin, R. Ramesh, Advances in magnetoelectric multiferroics, *Nature Materials*, 2019, **18**, 203–212.

[2] M. Bibes, A. Barthelemy, Multiferroics: Towards a magnetoelectric memory, *Nature Materials*, 2008, **7**, 425-426.

[3] J. Ma, J. Hu, Z. Li, C. W. Nan, Recent progress in multiferroic magnetoelectric composites: from bulk to thin films, *Advanced Materials*, 2011, **23**, 1062-1087.

[4] N. A. Benedek, J. M. Rondinelli, H. Djani, P. Ghosez, P. Lightfoot, Understanding ferroelectricity in layered perovskites: new ideas and insights from theory and experiments, *Dalton Transactions*, 2015, **44**, 10543-10558.

[5] H. Yan, H. Zhang, R. Ubic, M. J. Reece, J. Liu, Z. Shen, Z. Zhang, A Lead-Free High-Curie-Point Ferroelectric Ceramic, CaBi2Nb2O9, *Advanced Materials*, 2005, **17**, 1261-1265.

[6] B. H. Park, B. S. Kang, S. D. Bu, T. W. Noh, J. Lee, W. Jo, Lanthanum-substituted bismuth titanate for use in non-volatile memories, *Nature*, 1999, **401**, 682-684.

[7] N. Sharma, C. D. Ling, G. E. Wrighter, P. Y. Chen, B. J. Kennedy, P. L. Lee. Three-layer Aurivillius phases containing magnetic transition metal cations: Bi2−xSr2+x(Nb,Ta)2 +xM1−xO12, M=Ru4+, Ir4+, Mn4+, x≈0.5, *Journal of Solid State Chemistry*, 2007, **180**, 370-376.

[8] Z. Li, K. Tao, J. Ma, Z. Gao, V. Koval, C. Jiang, G. Viola, H. Zhang, A. Mahajan, J. Cao, M. Cain, I. Abrahams, C. Nan, C. Jia, H. Yan, Bi3.25La0.75Ti2.5Nb0.25(Fe0.5Co0.5)0.25O12, a single phase room temperature multiferroic, *Journal of Materials Chemistry C*, 2018, **6**, 2733-2740.

[9] N. A. Lomanova, M. I. Morozov, V. I. Ugolkov, V. V. Gusarov, Properties of aurivillius phases in the Bi4Ti3O12-BiFeO3 system, *Inorganic Materials*, 2006, **42**, 189-195.

[10] H. Zhao, H. Kimura, Z. Cheng, M. Osada, J. Wang, X. Wang, S. Dou, Y. Liu, J. Yu, T. Matsumoto, T. Tohei, N. Shibata, Y. Ikuhara, Large magnetoelectric coupling in magnetically short-range ordered Bi5Ti3FeO15 film, *Scientific Reports*, 2014, **4**, 5255.

[11] E. Jartych, T. Pikula, M. Mazurek, A. Lisinska-Czekaj, D. Czekaj, K. Gaska, J. Przewoznik, C. Kapusta, Z. Surowiec, Antiferromagnetic spin glass-like behavior in sintered multiferroic Aurivillius Bim+1Ti3Fem−3O3m+3 compounds, *Journal of Magnetism and Magnetic Materials*, 2013, **342**, 27-34.

[12] I. G. Ismailzade, V. I. Nesterenko, F. A. Mirishli, P. G. Rustamov, X-Ray and electrical studies of system Bi4Ti3O12-BiFeO3, *Soviet Physics Crystallography*, 1967, **12**, 400-468.

[13] A. Srinivas, S. V. Suryanarayana, G. S. Kumar, M. M. Kumar, Magnetoelectric measurements on Bi5FeTi3O15 and Bi6Fe2Ti3O18, *Journal of Physics: Condensed Matter*, 1999, **11**, 3335-3340.

[14] A. Srinivas, M. M. Kumar, S. V. Suryanarayana, T. Bhimasankaram, Investigation of dielectric and magnetic nature of Bi7Fe3Ti3O21, *Materials Research Bulletin*, 1999, **34**, 989-996

[15] A. Srinivas, D. -W. Kim, K. S. Hong, S. V. Suryanarayana, Study of magnetic and magnetoelectric measurements in bismuth iron titanate ceramic - Bi8Fe4Ti3O24, *Materials Research Bulletin*, 2004, **39**, 55-61.

[16] G. D. Sultanov, R. M. Mirzababayev, N. G. Guseinov, R. A. Mamedov, Combined Hyperfine Interaction in Bi9Ti3Fe5O27, *Fizika Tverdovo Tela*, 1978, **20**, 1888-1890.

[17] A. Y. Birenbaum, A. Scaramucci, C. Ederer, Magnetic order in four-layered Aurivillus phases, *Physical Review B*, 2017, **95**, 104419.

[18] V. Koval, I. Skorvanek, G. Viola, M. Zhang, C. Jia, H. Yan, Crystal chemistry and magnetic properties of Gd-substituted Aurivillius-type Bi5FeTi3O15 ceramics, *Journal of Physical Chemistry C*, 2018, **122**, 15733-15743.

[19] L. Keeney, C. Downing, M. Schmidt, M. E. Pemble, V. Nicolosi, R. W. Whatmore, Direct atomic scale determination of magnetic ion partition in a room temperature multiferroic material, *Scientific Reports*, 2017, **7**, 1737.

[20] E. Jartych, T. Pikula, K. Kowal, J. Dzik, P. Guzdek, D. Czekaj, Magnetoelectric Effect in Ceramics Based on Bismuth Ferrite, *Nanoscale Research Letters*, 2016, **11**, 234.

[21] J. Su, Y. Long, Q. Li, C. Lu, K. Liang, J. Li, L. Luo, L. Sun, X. Lu, J. Zhu, Room-temperature magnetoelectric coupling in Bi4LaFeTi3O15 multiferroic films, *Journal of Alloys and Compounds*, 2018, **747**, 1002-1007.

[22] Z. Li, J. Ma, Z. Gao, G. Viola, V. Koval, A. Mahajan, X. Li, J. Jia, C. Nan, H. Yan, Room temperature magnetoelectric coupling in intrinsic multiferroic Aurivillius phase textured ceramics, *Dalton Transactions*, 2016, **45**, 14049-14052.

[23] X. Mao, W. Wang, X. Chen, Y. Lu, Multiferroic properties of layer-structured Bi5Fe0.5Co0.5Ti3O15 ceramics, *Applied Physics Letters*, 2009, **95**, 082901.

[24] W. Wang, X. H. Wu, X. Y. Mao, X. B. Chen, Multiferroic properties of sol—gel derived Bi5Fe1-xCoxTi3O15 thin films, *Chinese Physics B*, 2011, **20**, 077701.

[25] S. Liu, S. Yan, H. Luo, L. Yao, Z. Hu, S. Huang, L. Deng, Enhanced magnetoelectric coupling in La-modified Bi5Co0.5Fe0.5Ti3O15 multiferroic ceramics, *Journal of Materials Science*, 2018, **53**, 1014-1023.

[26] Z. Yu, X. Meng, Z. Zheng, Y. Lu, H. Chen, C. Huang, H. Sun, K. Liang, Z. Ma, Y. Qi, T. Zhang, Room temperature multiferroic properties of rare-earth-substituted Aurivillius phase Bi5Ti3Fe0.7Co0.3O15 ceramics, *Materials Research Bulletin*, 2019, **115**, 235-241.

[27] X. Mao, H. Sun, W. Wang, X. Chen, Y. Lu, Ferromagnetic, ferroelectric properties, and magneto-dielectric effect of Bi4.25La0.75Fe0.5Co0.5Ti3O15 ceramics, *Applied Physics Letters*, 2013, **102**, 072904.

[28] X. Z. Zuo, M. L. Zhang, E. J. He, J. Yang, X. B. Zhu, J. M. Dai, Multiferroic property, dielectric response, and scaling behavior in Aurivillius Bi4.25Gd0.75Fe0.5Co0.5Ti3O15 ceramic, *Journal of Alloys and Compounds*, 2017, **695**, 2556-2562.

[29] D. L. Zhang, W. C. Huang, Z. W. Chen, W. B. Zhao, L. Feng, M. Li, Y. W. Yin, S. N. Dong, X. G. Li, Structure Evolution and Multiferroic Properties in Cobalt Doped Bi4NdTi3Fe1-xCoxO15-Bi3NdTi2Fe1-xCoxO12-δ Intergrowth Aurivillius Compounds, *Scientific Reports*, 2017, **7**, 43540.

[30] Z. Yu, B. Yu, Y. Liu, P. Zhou, J. Jiang, K. Liang, Y. Lu, H. Sun, X. Chen, Z. Ma, T. Zhang, C. Huang, Y. Qi, Enhancement of multiferroic properties of Aurivillius Bi5Ti3FeO15 ceramics by Co doping, *Ceramics International*, 2017, **43**, 14996-15001.

[31] S. Sun, Z. Chen, G. Wang, X. Geng, Z. Xiao, Z. Sun, Z. Sun, R. Peng, Y. Lu, Nanoscale Structural Modulation and Low-temperature Magnetic Response in Mixed-layer Aurivillius-type Oxides, *Scientific Reports*, 2018, **8**, 871.

[32] S. Sun, Y. Huang, G. Wang, J. Wang, Z. Fu, R. Peng, R. J. Knize, Y. Lu, Nanoscale structural modulation and enhanced room-temperature multiferroic properties, *Nanoscale*, 2014, **6**, 13494-13500.

[33] T. Žák, in: M. Miglierini and D. Petridis (Eds.), Mössbauer Spectroscopy in Materials Science, Kluwer Academic Publishers, Dordrecht, 1999, p. 385.

[34] J. J. Rehr, R. C. Albers, Theoretical approaches to x-ray absorption fine structure, *Reviews of Modern Physics*, 2000, **72**, 621-654.

[35] N. A. Lomanova, V. V. Gusarov, Phase states in the Bi4Ti3O12-BiFeO3 section in the Bi2O3-TiO2-Fe2O3 system, *Russian Journal of Inorganic Chemistry*, 2011, **56**, 616-620.

[36] PDF-2 database, http://www.icdd.com/pdf-2/

[37] M. I. Morozov, L. P. Mezentseva, V. V. Gusarov, Mechanism of Formation of Bi4Ti3O12, *Russian Journal of General Chemistry*, 2002, **72**, 1038-1040.

[38] R. Palai, R. S. Katiyar, H. Schmid, P. Tissot, S. J. Clark, J. Robertson, S. A. T. Redfern, G. Catalan, J. F. Scott, β phase and γ-β metal-insulator transition in multiferroic BiFeO3, *Physical Review B*, 2008, **77**, 014110.

[39] O. Jankovský, D. Sedmidubský, Z. Sofer, J. Čapek, K. Růžička, Thermal properties and homogenity range of Bi24+xCo2-xO39 ceramics, *Ceramics-Silikáty*, 2013, **57**, 83-86.

[40] V. R. Sastri, J.R. Perumareddi, V. R. Rao, G.V.S. Rayudu, J. -C. Bünzli, Modern aspects of Rare Earths and their Complexes, Elsevier Science, 2003, p. 378.

[41] V. G. Vlasenko, S. V. Zubkov, V. A. Shuvaeva, Structure and dielectric properties of Bi6-x SrxTi2-xNb2+xO18 (x = 0-2) solid solutions, *Physics of the Solid State*, 2013, **55**, 101−104.

[42] T. Wang, H. Deng, X. Meng, H. Cao, W. Zhou, P. Shen, Y. Zhang, P. Yang, J. Chu, Tunable polarization and magnetization at room-temperature in narrow bandgap Aurivillius Bi6Fe2−xCox/2Nix/2 Ti3O18, *Ceramics International*, 2017, **43**, 8792-8799.

[43] P. Hermet, M. Goffinet, J. Kreisel, P. Ghosez, Raman and infrared spectra of multiferroic bismuth ferrite from first principles, *Physical Review B*, 2007, **75**, 220102(R).

[44] S. Kojima, R. Imaizumi, S. Hamazaki, M. Takashige, Raman study of ferroelectric bismuth layer-oxides ABi4Ti4O15, *Journal of Molecular Structure*, 1995, **348**, 37-40.

[45] S. A.Ivanov, P. Nordblad, R. Tellgren, T. Ericsson, H. Rundlof, Structural, magnetic and Mössbauer spectroscopic investigations of the magnetoelectric relaxor Pb(Fe0.6W0.2Nb0.2)O3, *Solid State Sciences*, 2007, **9**, 440-450.

[46] N. A. Lomanova, V. G. Semenov, V. V. Panchuk, V. V. Gusarov, Structural changes in the homologous series of the Aurivillius phases Bin+1Fen−3Ti3O3n+3, *Journal of Alloys and Compounds*, 2012, **528**, 103-108.

[47] Y. W. Lu, C. C. Yan, M. X. Yu, C. X. Bing, The doping effects of BiFe1-xCoxO3 (x=0.0-0.8) in layered perovskite Bi4Ti3O12 ceramics, *Chinese Physics B*, 2012, **21**, 047502.

[48] J. Wang, Z. Fu, R. Peng, M. Liu, S. Sun, H. Huang, L. Li, R. J. Knize, Y. Lu, Low magnetic field response single-phase multiferroics under high temperature, *Materials Horizons*, 2015, **2**, 232-236.

[49] S. Kawano, N. Achiwa, N. Yamamoto, S. Higashi, Metal-ion distribution and magnetic structure of Fe-substituted cobaltite spinel: FeCo2O4, *Materials Research Bulletin*, 1976, **11**, 911-916.

[50] M. Ben Ali, K. El Maalam, H. El Moussaoui, O. Mounkachi, M. Hamedoun, R. Masrour, E. K. Hlil, A. Benyoussef, Effect of zinc concentration on the structural and magnetic properties of mixed Co–Zn ferrites nanoparticles synthesized by sol/gel method, *Journal of Magnetism and Magnetic Materials*, 2016, **398**, 20–25.

[51] M. Ben Ali, O. Mounkachi, K. El Maalam, H. El Moussaoui, M. Hamedoun, E. K. Hlil, D. Fruchart, R. Masrour, A. Benyoussef, Coexistence of blocked, metamagnetic and canted ferrimagntic phases at high temperature in Co–Nd ferrite nanorods, *Superlattices and Microstructures*, 2015, **84**, 165–169.

[52] J. Kanamori, Superexchange interaction and symmetry properties of electron orbitals. *Journal of Physics and Chemistry of Solids*, 1959, **10**, 87-98.

[53] D. Zhang, L. Feng, W. Huang, W. Zhao, Z. Chen, X. Li, Oxygen vacancy-induced ferromagnetism in Bi4NdTi3FeO15 multiferroic ceramics, *Journal of Applied Physics*, 2016, **120**, 154105.

[54] V. Koval, I. Skorvanek, J. Durisin, G. Viola, A. Kovalcikova, P. Svec Jr., K. Saksl, H. Yan, Terbium-induced phase transitions and weak ferromagnetism in multiferroic bismuth ferrite ceramics, *Journal of Materials Chemistry C*, 2017, **5**, 2669-2685.

[55] X. Zuo, S. Zhu, J. Bai, E. He, Z. Hui, P. Zhang, D. Song, W. Song, J. Yang, X. Zhu, J. Dai, Enhanced multiferroicity and narrow band gap in B-site Co-doped Aurivillius Bi5FeTi3O15, *Ceramics International*, 2019, **45**, 137-143.

[56] L.A. Grunes, Study of the K edges of 3d transition metals in pure and oxide form by x-ray-absorption spectroscopy, *Physical Review B*, 1983, **27**, 2111-2131.

[57] N. Jiang, D. Su, J. C. H. Spence, Determination of Ti coordination from pre-edge peaks in Ti K-edge XANES, *Physical Review B*, 2007, **76**, 214117.

[58] T. Yamamoto, Assignment of pre-edge peaks in K-edge x-ray absorption spectra of 3d transition metal compounds: electric dipole or quadrupole?, *X-ray Spectrometry*, 2008, **37**, 572-584.

[59] H. Wen, M. Sassi, Z. Luo, C. Adamo, D. G. Schlom, K. M. Rosso, X. Zhang, Capturing ultrafast photoinduced local structural distortions of BiFeO3, *Scientific Reports*, 2015, **5**, 15098.

[60] V. Kumar, Y. Kumar, R. Kumar, D. K. Shukla, S. K. Arora, I. V. Shvets, R. Kumar, Structural, magnetic and x-ray absorption studies of NdCo1−xNixO3 ($0 \leq x \leq 0.5$), *Journal of Applied Physics*, 2013, **113**, 043918.

[61] J. H. Lee, H. J. Choi, D. Lee, M. G. Kim, C. W. Bark, S. Ryu, M. Oak, H. M. Jang, Variations of ferroelectric off-centering distortion and 3d−4p orbital mixing in La-doped BiFeO3 multiferroics, *Physical Review B*, 2010, **82**, 045113.

[62] K. Binder, A. P. Young, Spin glasses: Experimental facts, theoretical concepts, and open questions, *Reviews of Modern Physics*, 1986, **58**, 801-976.

[63] Y. H. Chu, L. W. Martin, M. B. Holcomb, M. Gajek, S. J. Han, Q. He, N. Balke, C. H. Yang, D. Lee, W. Hu, Q. Zhan, P. L. Yang, A. Fraile-Rodríguez, A. Scholl, S. X. Wang, R. Ramesh, Electric-field control of local ferromagnetism using a magnetoelectric multiferroic, *Nature Materials*, 2008, **7**, 478-482.

[64] H. Béa, M. Gajek, M. Bibes, A. Barthélémy, Spintronics with multiferroics, *Journal of Physics: Condensed Matter*, 2008, **20**, 434221.

39

40

FIGURE CAPTIONS

Figure 1. (a) DSC curves of the BiG5 composition samples. Reaction kinetics of raw oxides upon heating, curve DSC(1) - black line, and TG curve – green line. Thermogram of the reacted powder upon cooling, curve DSC(2) - red line, with two distinct thermal events. (b) Ferroelectric phase transition temperatures of the BiG1-BiG5 samples, ferroelectric Curie temperatures, T_c^{FE}, as determined from the DSC curves.

Figure 2. The room-temperature XRD patterns of (a) BiG1, and (b) BiG4, as processed at three different temperatures – 1063 K, 1173 K and 1223 K (upper plot – peak positions of the experimental pattern of the sintered samples and reference main phase(s)/impurity; bottom plot - peak positions of the experimental pattern of the calcined powder and reference intermediate phases).

Figure 3. Rietveld plot for the refinement (a full-profile matching method) of (a) BFTO, (b) BiG1, (c) BiG2, (d) BiG3, (e) BiG4, and (f) BiG5. The allowed Bragg reflections for the corresponding space groups ($A2_1am$, $B2cb$ and $I23$) are marked by green, dark blue and pink ticks, respectively. Black open circles represent the observed data, red solid line is the calculated profile and blue solid line illustrates the difference between the observed and calculated data.

Figure 4. Stacked plot of Raman scattering spectra of the BiG1-BiG5 samples, as collected at room temperature (most significant changes induced by the substitution are marked by red arrows).

Figure 5. Fitted room-temperature Mössbauer spectra of BiG1, BiG3 and BiG5 (full red circles – total fit, pink and green doublets – paramagnetic contributions, blue sextet – hyperfine splitting). The inset illustrates the distribution of the hyperfine magnetic field induction for the BiG5 sample.

Figure 6. Field dependence of the magnetization of the BiG1-BiG5 samples, as recorded at (a) 300 K, and (b) 5 K. The insets show the enlarged sections of the M-H hysteresis loops within the selected low magnetic field region.

41

Figure 7. Temperature dependence of the magnetization of the BiG1-BiG5 samples, as collected at a magnetic field of 1000 Oe (the inset shows the magnetic transition temperatures of the respective samples).

Figure 8. STEM-HAADF images of (a) BiG3, (b) BiG1, and (c, d) BiG5. The orderly arranged bright spots represent bismuth atoms; the inset and red open ellipses in (a) confine the defect area in the mixed-layer structure, where the nanoscale structural modulation appears. The thicknesses of the pseudo-perovskite slabs in three- and four-layered phases is highlighted in (b) and (c). The disordered intergrowth of the two phases in the BiG5 sample is illustrated in (d).

Figure 9. XANES Fe K-edge spectra of the BiG1-BiG5 samples and reference powders of hematite (α-Fe$_2$O$_3$) and magnetite (Fe$_3$O$_4$), as collected at room temperature. The insets show a zoomed part of spectral peaks A and C.

Figure 10. Spin glass-like behavior of the phase-modulated Aurivillius samples at low temperatures. (a) Temperature dependence of the ZFC and FC magnetization of BiG1-BiG5, as measured at a field of 1000 Oe. (b) AC susceptibility of the BiG3 sample in the temperature interval of 120-350 K; the in-phase (real) and out-of-phase (imaginary) components of the susceptibility were collected at nine different frequencies between 0.1 Hz and 1000 Hz.

GRAPHICAL ABSTRACT
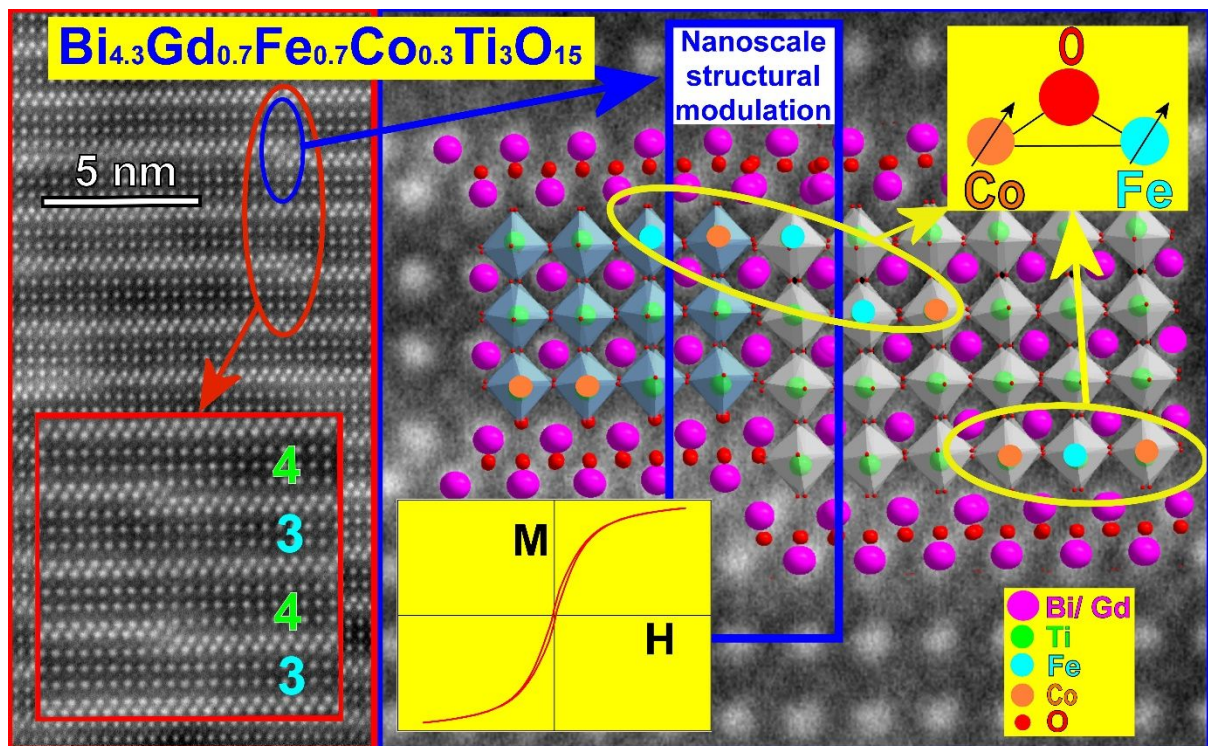
Supplementary material

Cobalt-induced structural modulation in multiferroic Aurivillius-phase oxides

V. Koval[1], Y. Shi[2], I. Skorvanek[3], G. Viola[4], R. Bures[1], K. Saksl[1], P. Roupcova[5,6], M. Zhang[4], Ch. Jia[2], and H. Yan[4]

[1]Institute of Materials Research, Slovak Academy of Sciences, Kosice, Slovakia

[2]Key Laboratory for Magnetism and Magnetic Materials of MOE, Lanzhou University, China

[3]Institute of Experimental Physics, Slovak Academy of Sciences, Kosice, Slovakia

[4]School of Engineering and Materials Science, Queen Mary University of London, United Kingdom

[5]Institute of Physics of Materials ASCR, Brno, Czech Republic

[6]CEITEC Brno University of Technology, Brno, Czech Republic
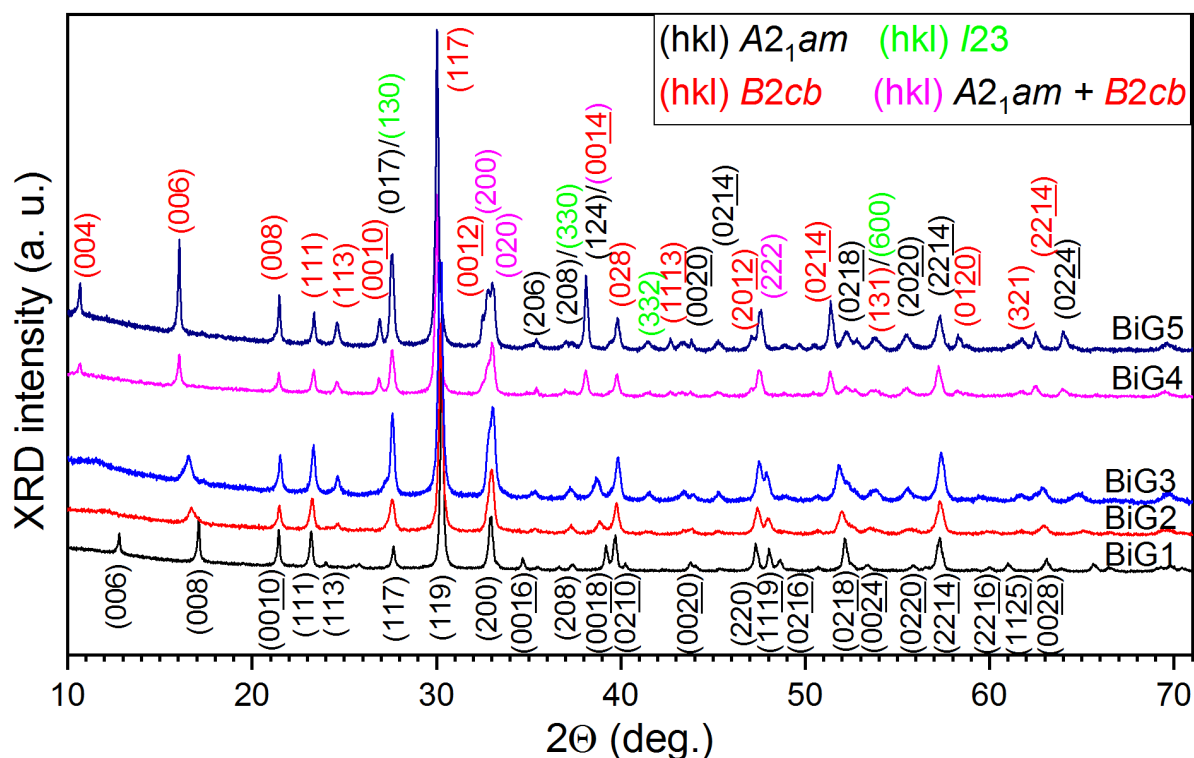
X-ray diffraction analysis

Figure S1. Stack plot of the XRD patterns of the BiG1-BiG5 samples, as recorded at room temperature (black Miller h, k, l indices: orthorhombic $A2_1am$ phase, red indices: orthorhombic $B2cb$ phase, green indices: cubic $I23$ phase; cyan indices: overlapped peaks of the $A2_1am$ and $B2cb$ phases).
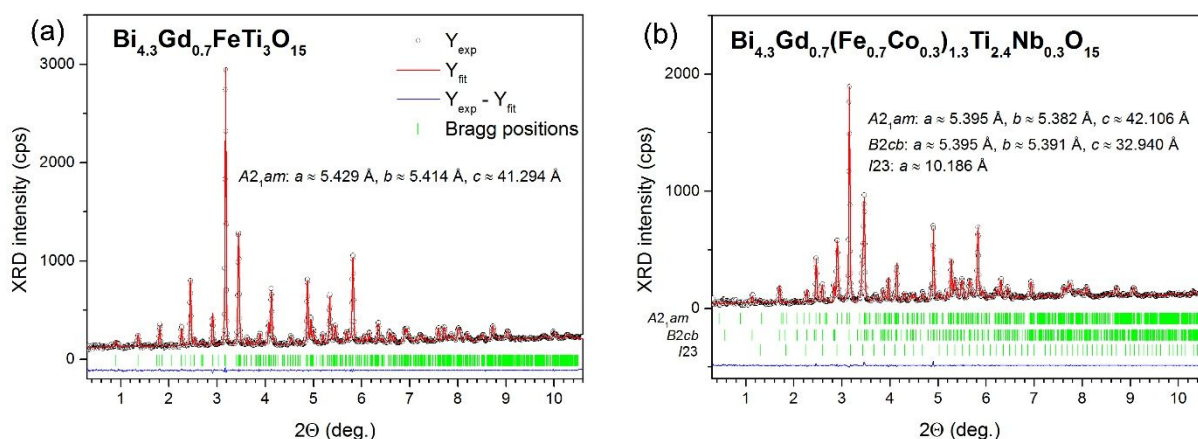
Figure S2. Observed (black open circles), calculated (red solid line) and difference (blue solid line) patterns obtained from the Rietveld analysis of the synchrotron XRD data of (a) BiG1, and (b) BiG4.

Table S1. The refined lattice parameters of the Aurivillius-phase samples, as obtained from the room temperature XRD data.

Sample/ phase	Lattice parameters				GOF
	a (Å)	b (Å)	c (Å)	V (Å^3)	χ^2
BFTO/A2$_1$am	5.4592(1)	5.4327(1)	41.2204(9)	1222.55(5)	1.28
BiG1/A2$_1$am	5.4302(1)	5.4121(1)	41.2628(6)	1212.68(3)	1.32
BiG2/A2$_1$am	5.414(1)	5.405(1)	41.562(1)	1216.21(6)	2.66
/B2cb	5.433(6)	5.407(3)	32.902(2)	966.54(5)	
BiG3/A2$_1$am	5.413(1)	5.394(0)	41.709(1)	1217.81(3)	2.73
/B2cb	5.431(4)	5.403(2)	32.933(12)	966.38(3)	
BiG4/A2$_1$am	5.414(0)	5.401(1)	41.614(9)	1216.83(2)	2.46
/B2cb	5.431(1)	5.401(2)	32.929(2)	965.90(3)	
BiG5/A2$_1$am	5.393(1)	5.383(1)	42.092(9)	1221.96(5)	2.74
/B2cb	5.399(1)	5.391(0)	32.940(2)	958.75(3)	

a, b and c – the lattice parameters, V – the unit cell volume, χ^2 – the goodness of fit (GOF)

Table S2[1]. Refined structural parameters and selected bond distances and bond angles for the 4-layered $A2_1am$ and 3-layered $B2cb$ Aurivillius phases, as obtained by Rietveld refinement of the room-temperature synchrotron XRD data of the BiG1 and BiG4 samples.

$A2_1am$	$a = 5.4292(4)$ Å, $b = 5.4146(4)$ Å, $c = 41.294(2)$ Å, $V = 1213.9(1)$ Å^3				
Atom	**Wyckoff positions**	**Fractional Coordinates**			**U$_{iso}$ (x 100) (Å^2)**
		x	y	z	
Bi/Gd(1)	4a	0.25[a]	0.247(5)	0	1.03(4)
Bi/Gd(2)	8b	0.235(8)	0.243(2)	0.1043(1)	1.61(2)
Bi(3)	8b	0.231(5)	0.267(3)	0.2189(1)	1.36(2)
Ti/Fe(1)	8b	0.292(6)	0.247(9)	0.4511(4)	0.63[b]
Ti/Fe(2)	8b	0.270(9)	0.255(9)	0.3469(4)	0.63[b]
O(1)	4a	0.320[c]	0.190[c]	0.5[c]	0.42[b]
O(2)	8b	0.616[c]	0.539[c]	0.0525[c]	1.56[b]
O(3)	8b	0.300[c]	0.310[c]	0.4005[c]	0.91[b]
O(4)	8b	0.490[c]	0.480[c]	0.1357[c]	0.72[b]
O(5)	8b	0.306[c]	0.226[c]	0.3066[c]	1.72[b]
O(6)	8b	0.525[c]	0.467[c]	0.2434[c]	0.56[b]
O(7)	8b	0.011[c]	0.970[c]	0.0403[c]	1.47[b]
O(8)	8b	0.040[c]	0.037[c]	0.1487[c]	0.55[b]

Bond lengths (Å):

Bi/Gd(1)-O(1)	2.36(5)	Bi(1)-O(2)	2.56(2)	Bi(1)-O(7)	2.48(1)
	2.43(5)		3.34(5)		2.59(3)
	3.04(7)				
	3.11(7)				
Bi/Gd(2)-O(2)	2.52(1)	Bi(2)-O(3)	2.38(7)	Bi(2)-O(4)	2.34(6)
	3.38(1)		3.09(4)		2.43(8)
				Bi(2)-O(7)	3.25(8)
Bi(3)-O(5)	2.53(7)	Bi(3)-O(6)	2.09(4)	Bi(2)-O(8)	2.39(4)
	2.73(6)		2.17(8)		2.89(9)
	3.14(1)		2.30(8)		
	3.30(4)		2.76(8)	Bi(3)-O(8)	3.32(1)
Bi(3)-Bi(3)	3.71(2)	O(6)-O(6)	2.73(2)		

Bond angles (deg.):

O(3)-O(1)-O(3)	161.8(2)		O(1)-O(3)-O(5)	164.2(3)
O(7)-O(2)-O(7)	150.6(3)		O(8)-O(4)-O(8)	148.9(1)

Ti/Fe(1)-O(1)-Ti/Fe(1)	160.6(6)	Ti/Fe(1)-O(3)-Ti/Fe(2)	162.2(3)
Ti/Fe(1)-O(7)-Ti/Fe(1)	155.1(2)	Ti/Fe(2)-O(8)-Ti/Fe(2)	162.9(2)

Octahedral tilts (deg.):

O(1)-O(3):O(6)-O(6)	9.1(2)	O(3)-O(5):O(6)-O(6)	6.7(2)

R-factors: $R_w = 6.4$, $R_p = 9.2$

---

[1] A slight difference in lattice parameters obtained by full profile matching method and those refined using the Rietveld method is brought by the different X-ray sources used (standard laboratory unit *vs*. high-energy synchrotron source), providing distinctive accuracy and resolution, specifically, for determining oxygen positions in bismuth-layered Aurivillius structures.

3

Table S2 (cont.)

$B2cb$	$a = 5.3994(8)$ Å, $b = 5.3907(7)$ Å, $c = 32.940(2)$ Å, $V = 958.8(2)$ Å^3			
Atom	**Wyckoff positions**	**Fractional Coordinates**		**U_{iso} (x 100)**
		x	y	z	(Å^2)
Bi(1)/Gd(1)	8b	0.13511[a]	0.994(9)	0.0659(2)	2.5(3)
Bi(2)	8b	0.150(16)	0.015(8)	0.2098(2)	1.9(2)
Ti/Fe/Co/Nb(1)	4a	0.100(13)	0	0.5	0.6[b]
Ti/Fe/Co/Nb(2)	8b	0.125(15)	0.96(2)	0.3719(5)	0.6[b]
O(1)	8b	0.3207[d]	0.2299[d]	0.0057[d]	1.5[b]
O(2)	8b	0.3783[d]	0.2527[d]	0.2519[d]	1.5[b]
O(3)	8b	0.0839[d]	0.0605[d]	0.4406[d]	1.5[b]
O(4)	8b	0.0931[d]	0.9700[d]	0.3174[d]	1.5[b]
O(5)	8b	0.3804[d]	0.2674[d]	0.1115[d]	1.5[b]
O(6)	8b	0.3209[d]	0.2216[d]	0.8793[d]	1.5[b]

Bond lengths (Å):

Bi/Gd(1)-O(1)	2.53(6)	Bi/Gd(1)-O(3)	2.41(3)	Bi/Gd(1)-O(6)	2.39(7)
	2.85(8)		3.46(6)		2.91(7)
	2.97(9)				
Bi(2)-O(2)	2.27(2)	Bi(2)-Bi(2)	3.70(2)	Bi(2)-O(4)	2.61(11)
	3.31(6)	O(2)-O(2)	2.72(3)		2.97(4)

Bond angles (deg.):

O(3)-O(3)-O(4)	163.7(4)			O(1)-O(1)-O(1)	164.1(2)
Ti/Fe(1)-O(3)-Ti/Fe(1)	158.4(1)	Ti/Fe(2)-O(3)-Ti/Fe(2)	158.4(1)		
Ti/Fe(1)-O(1)-Ti/Fe(1)	160.0(2)	Ti/Fe(2)-O(5)-Ti/Fe(2)	143.3(5)		

Octahedral tilts (deg.):

O(3)-O(3):O(2)-O(2)	9.4(1)	O(3)-O(4):O(2)-O(2)	6.9(1)

R-factors:	$R_w = 11.4$, $R_p = 16.6$

[a]Fixed to define origin of polar axis.
[b]U_{iso} fixed as Rietveld refinement tends towards negative values.
[c]Oxygen coordinates taken from *Ref.* [18].
[d]Oxygen coordinates taken from *Ref.* [8].

Notes to the Rietveld analysis of the XRD data and Table S2:

The initial structural data for the four-layered $A2_1am$ phase in BiG1 and the three-layered $B2cb$ phase in BiG4 were taken from our previous studies on Gd-substituted BFTO [18] and multiferroic $Bi_{3.25}La_{0.75}(Fe_{0.5}Co_{0.5})_{0.25}Ti_{2.5}Nb_{0.25}O_{12}$ ceramics [8], respectively. The B-site cations were set to occupy the same position in the centre of each oxygen octahedron in the perovskite-like layers with fixed Ti occupancy (3/4 in $A2_1am$ phase and nearly 1/2 in $B2cb$ phase). The occupancies of Fe, Co and Nb were adjusted in the refinement of both phases in

4

the way to reflect the nominal doping level of the Co and Nb ions. The isotropic atomic displacement parameters (ADPs) of these ions were constrained to be equivalent. The positions of oxygens with ADPs in both structures were taken from *Refs.* [8,18] and not further refined in order to stabilize the refinements. It is worth mentioning that in the doped samples, the accuracy of the refinement decreased by an order due to the structural similarity of the main orthorhombic phases $A2_1am$ and $B2cb$. Also, the values of the GOF parameter are about twice of the value of the single phase BiG1, although they are yet representing a good match between experimental and calculated XRD patterns.

From the modelled crystal structure (Figs. S4(a) and S4(b)) of $Bi_{4.3}Gd_{0.7}FeTi_3O_{15}$ and $Bi_{4.3}Gd_{0.7}(Fe_{0.5}Co_{0.5})_{1.3}Ti_{2.4}Nb_{0.3}O_{15}$, the size of perovskite-like slabs, the *a* parameter, in the four- and three- layered Aurivillius phases was estimated to be ~4.307 Å and ~4.335 Å, respectively. The fluorite-like $(Bi_2O_2)^{2+}$ layer remains in both the four- and three-layered Aurivillius phases practically identical within the range of the experimental error (the Bi-Bi bond length is about 3.7 Å and the distance between oxygen ions is about 2.7 Å). Therefore, since the unconstrained *a* parameter of the fluorite-like $(Bi_2O_2)^{2+}$ layer in both the four- and three-layered Aurivillius phases does not change (~3.70 Å), this suggests that the perovskite-like slabs of the $B2cb$ phase in the BiG5 sample are under larger compressive stress than those of the $A2_1am$ phase. As a result, the larger size mismatch between perovskite-like slabs and fluorite-like layers (interlayer mismatch) in the doped samples is relieved by the larger tilting distortion of the oxygen octahedra. The comparison of the non-bonded contact angles O3-O1-O3 in $A2_1am$ (~161.8[0]) and O3-O3-O4 in $B2cb$ (~163.7[0]) indicates that the tilting around the *a*-axis in the four-layered phase is again smaller than that in the three-layered phase. On the other hand, the bond angles of the B-O-B chains along the *c*-axis in the inner and outer perovskite-like layers are smaller in the three-layered structure, if compared to those of the four-layered phase.

By comparing the values of Bi-O bond lengths in the *ab* plane for the four- and three-layered structures (Table S2), one can see that the distance between bismuth and oxygen atoms in $B2cb$ (Bi1-O3) is about 2% longer than that in the $A2_1am$ phase (Bi1-O1≈2.36 Å). The longer Bi-O bond lengths in the *ab* plane and the smaller B-O-B bond angles along the *c*-axis in the three-layered Aurivillius phase suggest that the local environment of B-site cations in the inner perovskite-like slabs of the $B2cb$ structure differs from that in the $A2_1am$ structure. These findings are supportive of the inherent mechanism of lowering crystal symmetry driven by Co-doping of Gd-substituted BFTO (SG: $A2_1am$), which is accompanied by the occurrence and

5

growth of the three-layered *B2c* phase with the increased octahedral tilting. The introduction of the donor Nb ions at the B-sites of perovskite-like layers balances the electrical neutrality disrupted by Co doping, favouring the three-layered BTO-like Aurivillius phase.

Mössbauer spectra analysis

Table S3. Hyperfine interactions parameters of BiG1, BiG3 and BiG5 ceramics, as obtained from the numerical fitting of the Mössbauer spectra collected at 300 K.

Sample	Component	IS (mm/s)	QS (mm/s)	Δ (mm/s)	B_{eff} (T)	A (%)
BiG1	Doublet D1	0.35	0.50	-	-	90.4
	Doublet D2	0.25	0.72	-	-	9.6
BiG3	Doublet D1	0.29	0.27	-	-	56
	Doublet D2	0.21	0.71	-	-	43
	Sextet	0.26	-	0.08	40.3	1
BiG5	Doublet D1	0.28	0	-	-	19
	Doublet D2	0.23	0.65	-	-	47
	Sextet	0.29	-	-0.04	43.5	34

IS – isomer shift relative to α-iron, QS – quadrupole splitting of the doublet, Δ - quadrupole shift of the sextet, B_{eff} – effective hyperfine magnetic field induction, A – integral intensities ratio
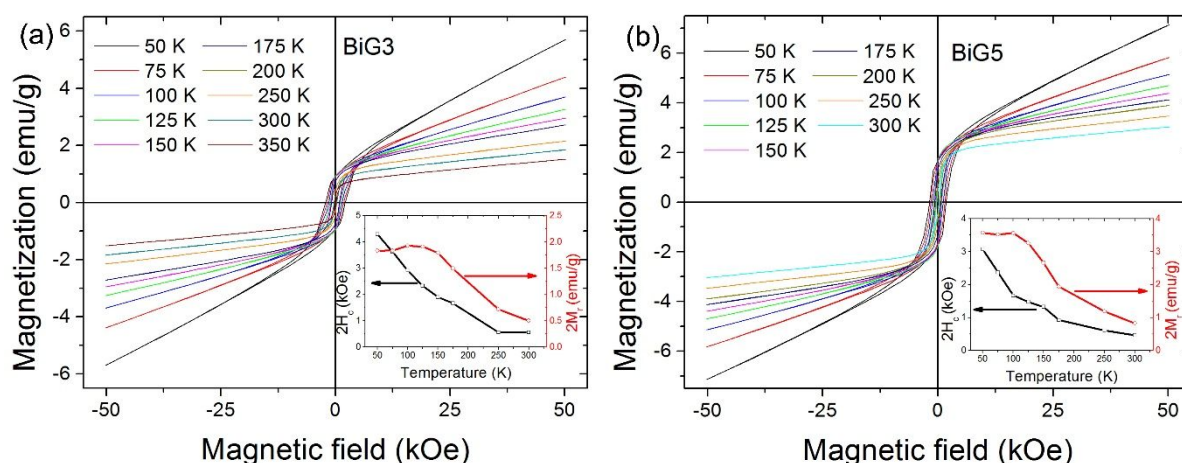
SQUID magnetometry

Figure S3. The magnetization *vs*. magnetic field hysteresis loops of (a) BiG3, and (b) BiG5, as recorded at different temperatures between 50 K and 350 K. The insets show the temperature dependences of the remanent magnetization ($2M_r$) and coercive field ($2H_c$) for the respective samples.
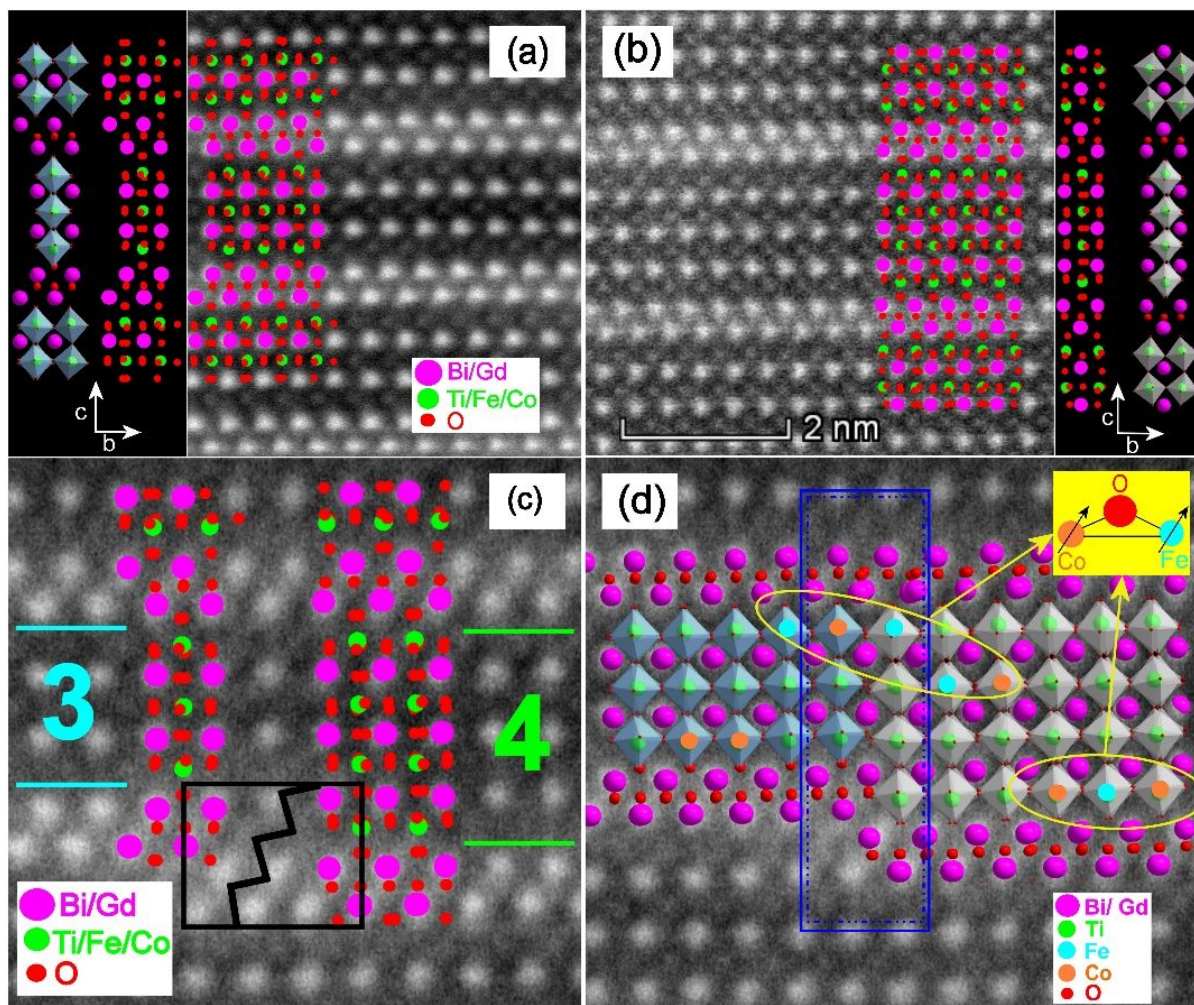
6

S-TEM HAADF imaging

Figure S4. Atomic scale resolution images of (a) the three-layered *B2cb* phase, and (b) the four-layered *A2₁am* phase (overlapped by the respective 2D and 3D sketches of the crystal structure). (c) The enlarged HAADF image nearby the Bi_2O_2 layer defect demonstrating the intergrowths of the three- and four-layered phases. (d) The illustration of the ferromagnetic Fe-O-Co clustering driven by the nanoscale structural modulation at the interface of the two phases.

7

NEXAFS and EXAFS analysis
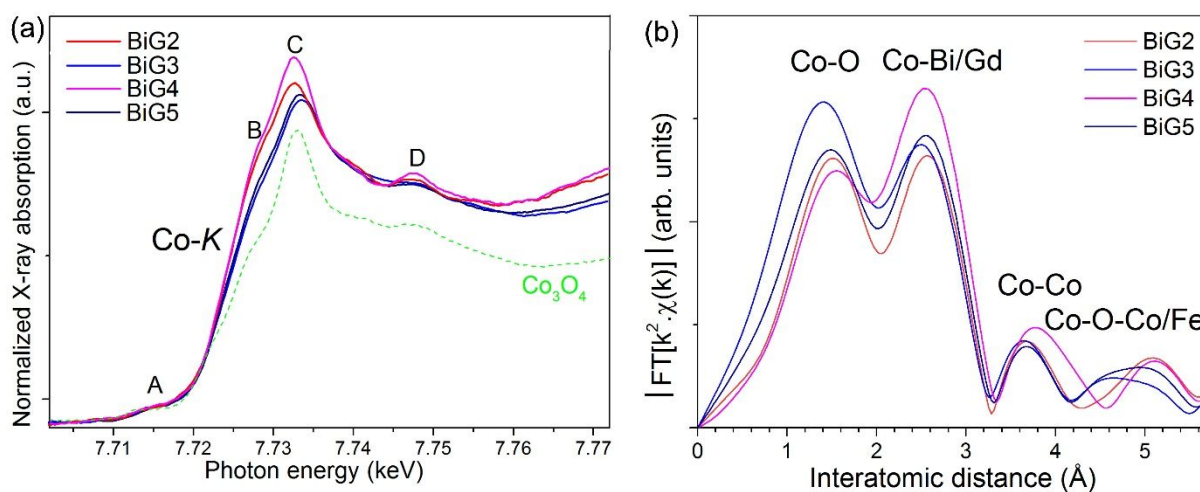
Figure S5. (a) The room-temperature XANES Co *K*-edge spectra of the BiG1-BiG5 samples. (b) Fourier transform (FT) of the EXAFS function, $\chi(k)$, into real space for the BiG1-BiG5 samples.
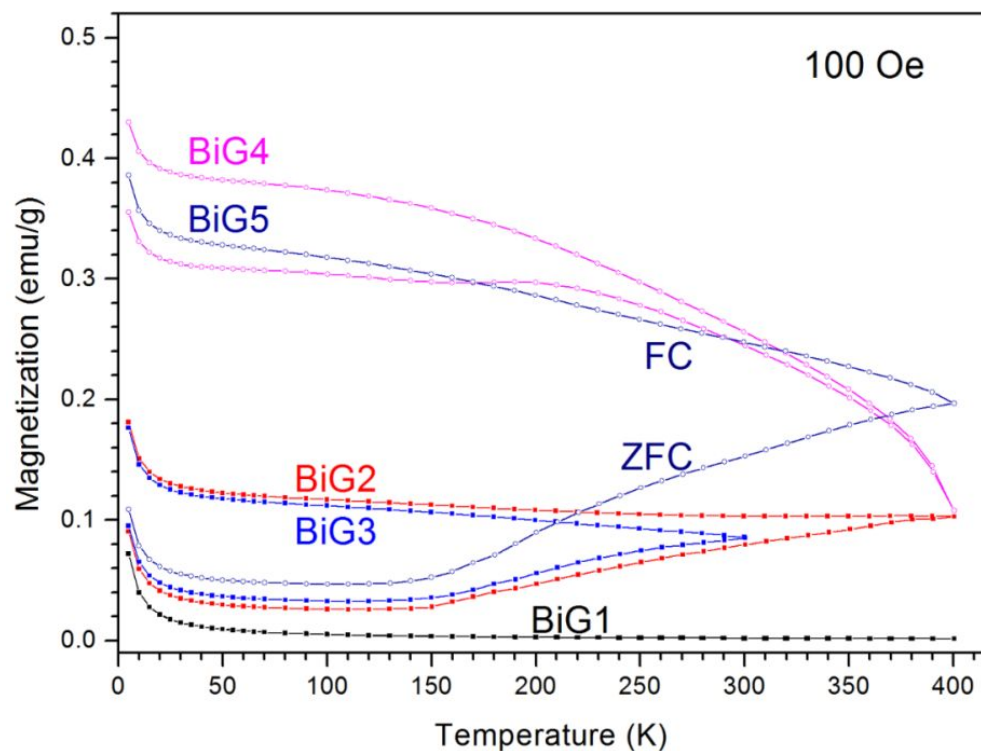
ZFC/FC magnetization

Figure S6. Magnetization as a function of temperature of the BiG1-BiG5 samples, as recorded at 100 Oe in the temperature range of 5 K-400 K.

Scanning electron microscopy analysis

Fig. S8(a) and S8(b) show cross-sectional SEM images of the polished, chemically etched surfaces of BiG1 and BiG5 ceramics, respectively. From the figure, one can see that both samples are formed of plate-like grains, characteristic of Aurivillius-phase materials [5]. The growth habit is determined by the particular crystalline (layered) structure which promotes preferential growth of grains in directions perpendicular to the stacking c-axis of the perovskite-like layers. In addition, the platelets of BiG1 ceramics are much smaller (the average length and width are about 1-1.5 μm and 0.2-0.3 μm, respectively) than those of BiG5 ceramics (average length: 4-5 μm and average width: 1 μm), indicating that the Co substitution and Co/Nb-codoping can effectively promote the grain growth in BFTO-derived materials. It should be noted that the Gd, Fe, Co and Nb elements also exist in the three-layered structure, implying that the $B2cb$ phase is not pure $Bi_4Ti_3O_{12}$ but rather of the $(Bi,Gd)_4(Ti,Nb)_2(Fe,Co)O_{12-\delta}$-type compound.
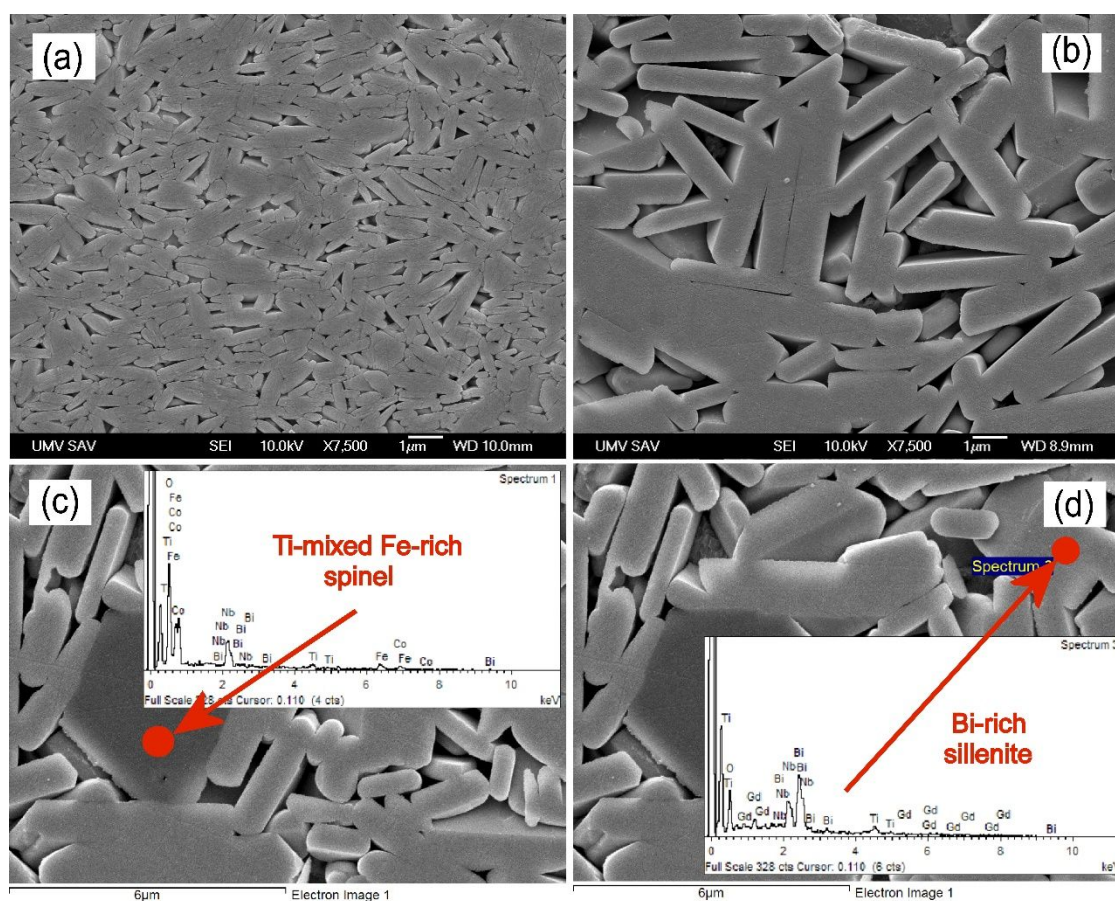

Figure S7. SEM images of (a) BiG1, and (b) BiG5 ceramics (magnification: x7500). (c, d) The micrograph demonstrating at a higher magnification (x20000) the existence of two different types of impurities in the BiG5 ceramics; (c) Ti-mixed Fe-rich spinel ferrite, and (d) Bi-rich sillenite-type particle. The insets of (c) and (d) are the EDX spectra of the impurities.

9

The presence of two different types of secondary phases in the doped BiG5 sample is evidenced in the micrographs obtained at a higher magnification (Fig. S8(c) and S8(d), magnification: 20000x). While the volume fraction of the cubic impurities (dark particles, size ~ 3-4 μm) is less than 3.5% (estimated from a series of micrographs, not shown here), i.e., below the detection limit of the XRD technique, the smaller octahedral-like shaped particles of about 2 μm occupy nearly 10 vol.% of the doped sample. Following the results of our XRD analysis, the latter impurities are supposed to be Bi-rich sillenite-type particles with composition close to $Bi_{12}TiO_{20}$. Semi-quantitative EDX analysis (spot scan), indeed, confirmed that the atomic ratio of the A-site cations (Bi+Gd) to the B-site cations (Ti+Nb) in these particles is about 12:1.

The atomic ratio Co/(Fe+Ti) in the dark cubic particles was found to be close to 1, suggesting that these impurities are Ti-mixed Fe-rich spinel ferrites ($FeCo_2O_4$-like spinels) Surprisingly, the EDX analysis of the dark particles in the ceramic samples with the lower concentration of the Co added (BiG2 and BiG4 ceramics) showed that the amount of Fe atoms is almost twice of Co atoms, which indicates that a minor secondary phase in these samples is of the spinel Fe_2CoO_4-type with Fe partially replaced by the Ti atoms. The presence of spinel-type impurities in the Co-doped four-layered Aurivillius compounds has been reported in our earlier work on La-BFCT ceramics [22] and also by other research groups [19,26,32].

AC magnetic susceptibility and spin glass-like behavior

The low frequency (0.1 Hz) AC susceptibility anomaly (see Fig. 10(b)) coincides with the temperature at which the DC magnetization starts to fall (see Fig. 10(a)), thus, we define the peak point in χ''_{ac} curve as the dynamic spin freezing temperature $T_f(\omega)$. The frequency dependence of T_f is often quantified by an empirical parameter ϕ:

$$\emptyset = \frac{\Delta T_f}{T_f \Delta log_{10}(\omega)}, \tag{1}$$

which represents the relative shift of T_f per decade of $\omega/2\pi$ on a logarithmic scale. The calculated value of the parameter ϕ for the BiG3 sample is about 0.083 and compares well with the values of 0.06 in certain shape memory alloys showing the SG state [65] and 0.095 reported in disordered SG systems such as $LaCo_{0.5}Ni_{0.5}O_3$ [66]. Accordingly, it can be proposed that the

10

initial frequency shift of 0.083 better characterizes our Aurivillius system as the so called cluster glass. In such a system of spin-clusters, a strong inter-cluster interaction can give rise to spin glass-like cooperative freezing at the critical spin-glass temperature T_{SG}, which is associated with the characteristic time $t=1/\omega$ (t corresponds to the maximum relaxation time τ, $\tau=2\pi/\omega$). Thus, as $\omega\rightarrow0$, $T_f(\omega)$ is expected to settle down to a "static limit", T_{SG}.
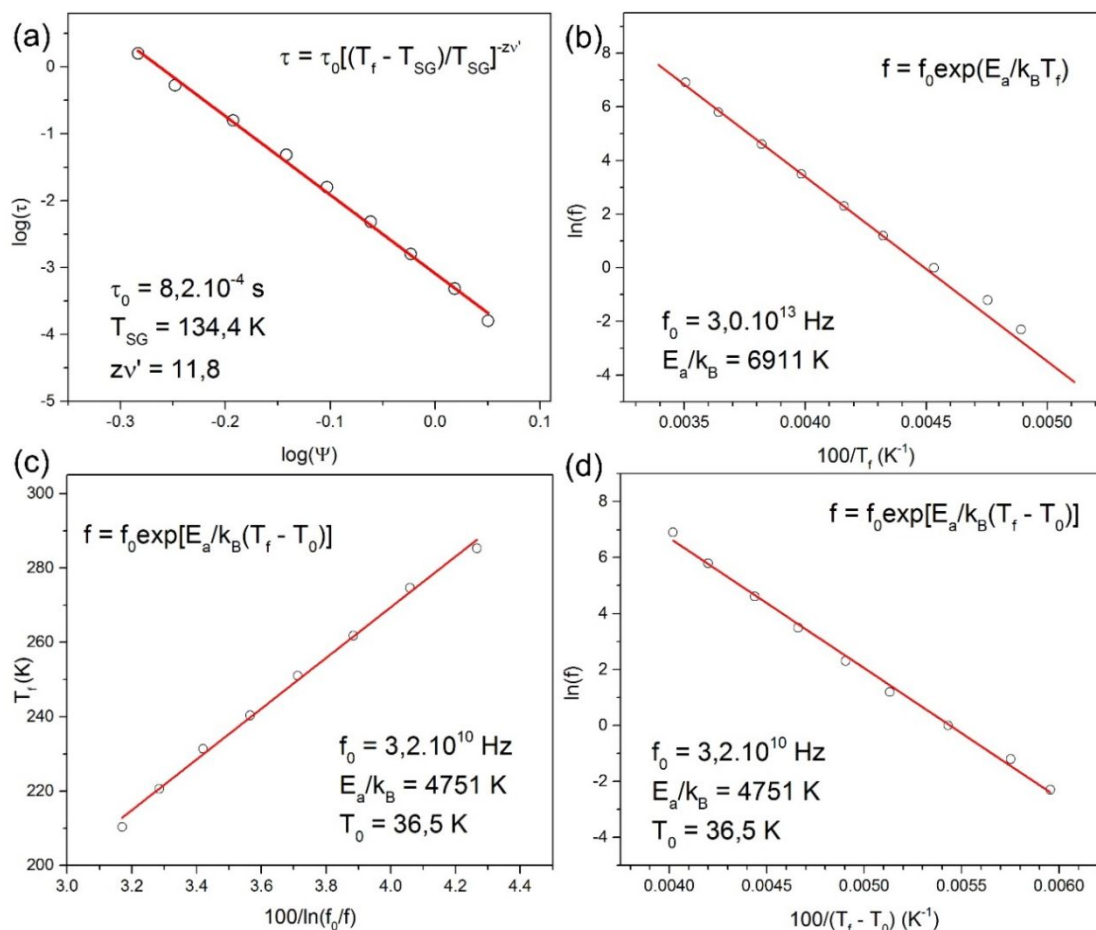

Figure S8. (a) The frequency dependence of freezing temperature plotted as $\log(\tau)$ vs. $\log(\psi)$, where the reduced temperature $\psi = (T_f\text{-}T_{SG})/T_{SG}$. The red solid line represents the fit to the power law divergence. (b) The frequency dependence of freezing temperature plotted as $\ln(f)$ vs. $100/T_f$. The red solid line represents the fit to the Arrhenius law. (c) The frequency dependence of freezing temperature plotted as T_f vs. $100/\ln(f_0/f)$. The red solid line represents the fit to the Vogel-Fulcher lav. (d) The frequency dependence of freezing temperature plotted as $\ln(f)$ vs. $100/(T_f\text{-}T_0)$. The red solid line represents the fit to the Vogel-Fulcher law.

On further analysis of the AC data, in the vicinity of T_{SG}, the T_f was found to obey the critical slowing down dynamics governed by the relation:

$$\tau = \tau_0 \left(\frac{T_f}{T_{SG}} - 1\right)^{-zv'},$$
(2)

where τ_0 is the shortest relaxation time available to the system, T_{SG} is the critical SG transition temperature, z is the dynamic critical exponent, and v' is the critical exponent of the correlation length. For a convenience, it is useful to rewrite Eq. 2 to the equivalent linearized form as:

$$ln(\tau) = ln(\tau_0) - zv'ln(\psi),$$
(3)

where $\psi=(T_f-T_{SG})/T_{SG}$. The slope and intercept of $ln(\tau)$ vs. $ln(\psi)$ plot can, thus, be used to estimate τ_0 and zv'. A log-log plot of inverse frequency (τ) vs. reduced temperature (ψ) of BiG3 is shown in Fig. S8(a). The value of T_{SG} was determined by extrapolating the T_f vs. $f^{1/zv'}$ to zero frequency, which gives T_{SG}=134.4 K (see the inset of Fig. S9). The solid red line in Fig. S8(a) represents the fit to the power law divergence (Eq. 2). The best fit to the experimental data (solid circles in Fig. S8(a)) yields the following fitting parameters: τ_0=8.2×10^{-4} s, T_{SG}=134.4 K and zv'=11.8. Fig. S9 clearly demonstrates the validity of the power law (green dashed line) over the whole experimental temperature range. The value of the critical dynamical exponent zv' is in good agreement with that reported for cluster glasses.[67,68] In addition, rather large τ_0 suggests a cluster-glass nature of the Aurivillius material, too. The slower relaxation, if compared to a conventional spin glass ($\tau_0 \sim$ 10^{-10}-10^{-13} s [62]), indicates that the low-temperature SG-like phase of BiG3 is composed of randomly distributed ferromagnetic clusters. Similar cluster glass effect, induced by disorder, has been reported in doped manganites and nanocrystalline alloys.[69,70]

The cooperative dynamics due to the inter-cluster interactions is also evident from the departure of the frequency dependence of T_f from the Néel-Arrhenius law (see Fig. S9, red dashed line) given by

$$\tau = \tau_0 exp\left(\frac{E_a}{k_B T_f}\right),$$
(4)

where E_a is the activation energy and k_B is the Boltzmann constant. A significant deviation from the expected linear behaviour at low frequencies confirms that the dynamics is not simply associated with single-spin flips, but rather reflects a cooperative character of the freezing process. We made an attempt to estimate the activation energy E_a by fitting the data above 10

12

Hz (red solid line in Fig. S8(b)) by an Eq. 4, yielding E_a/k_B=7876±188 and τ_0=5.3×10^{-15} s which are totally unrealistic values.
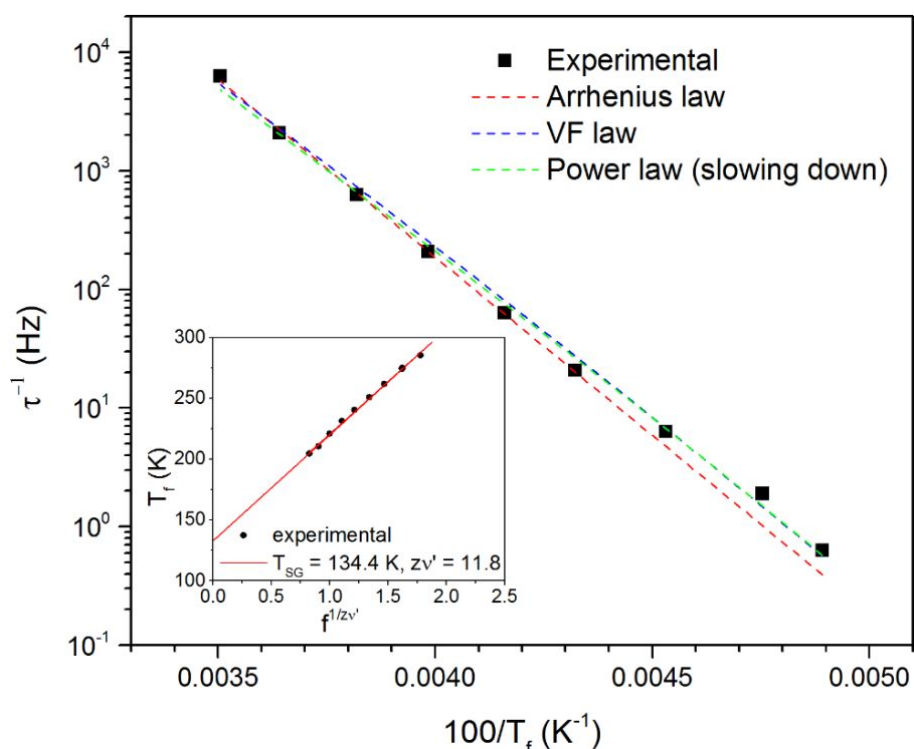

Figure S9. Fitting the χ''_{ac} maxima by the Arrhenius law (red dashed line), the Vogel-Fulcher law (blue dashed line) and the power law (Eq. 2, green dashed line). The straight line in the inset defines the value of the critical exponent zv' and the critical spin-glass temperature T_{SG}.

On the other hand, the empirical Vogel-Fulcher law [62] which takes into account the interactions among spin clusters:

$$\tau = \tau_0 exp\left(- \frac{E_a}{k_B(T_f - T_0)} \right), \tag{5}$$

where T_0 is the Vogel-Fulcher temperature which represents the measure of inter-cluster interaction strength and describes the relaxation behaviour in the vicinity of the SG-like transition satisfactorily, as shown in Fig. S8(c) and S8(d). A good linear fit of the Vogel-Fulcher law to the experimental data with physically meaningful parameters τ_0=3.1x10^{-11} s, T_0=36.5 K and E_a=0.41 eV was obtained from the slope and intercept of T_f vs. $1/ln(f_0/f)$ plot. According to the criterion introduced by Tholence [71], $T^*=(T_f-T_0)/T_f$ should be very small for SG states. Our value of T^* for the BiG3 sample is about 0.82, which is an order magnitude higher than those

13

reported for canonical spin glasses or ideal spin glasses [62], but is comparable to the values obtained for systems with a progressive freezing of clusters [72].

From the AC susceptibility analysis, one can infer that the glassy magnetic behavior of the Aurivillius compounds originates from competing antiferromagnetic and ferromagnetic interactions within and between the cooperative Fe-O-Co polar clusters, which support the presence of Co^{3+} ions in the low spin (LS) state, Co^{3+} ($S=0$). According to Goodenough-Kanamori rules for super-exchange interactions [52], a disordered distribution of LS Co^{3+} and high spin Fe^{3+} would result in the frustration between the ferromagnetic double exchange (Co-Fe) and the antiferromagnetic superexchange (Co-Co and Fe-Fe) interactions. The presence of low concentrations of Co^{2+}, as indicated by the XAFS study, in the high spin ($S=3/2$) electronic configuration further rationalize the spin glass behavior at low temperatures, as the HS Co^{2+} - HS Co^{2+}, HS Co^{2+} - LS Co^{3+} interactions are antiferromagnetic [52].

Dielectric and ferroelectric properties

To investigate the dielectric behaviour of the Aurivillius materials near the Curie point and at the same time to confirm the temperature of the ferroelectric-to-paraelectric phase transition determined by DSC, we performed the dielectric property measurements in a temperature window of 800 K – 1200 K.

For dielectric and ferroelectric characterization, the sintered pellets were first thinned to a thickness of about 0.5 mm by wet grinding (#1200 SiC paper, Struers GmbH, Germany) followed by polishing (DP-Suspension P, Struers GmbH, Germany), and then major faces of the disks were electroded with fired-on silver paste (#7095, DuPont Ltd., UK). The dielectric properties were measured using a precision impedance analyzer (#4294A, Agilent, Japan) attached to a home-made laboratory furnace. Ferroelectric characterization was performed with a ferroelectric tester (NPL, Teddington, UK) with the testing frequency of a triangular voltage waveform of 10 Hz.

Fig. S10 shows the temperature dependencies of the relative dielectric permittivity (ε_r) of the Co-free BiG1 sample and the representative Co-doped and Co/Nb- codoped ceramics (BiG2, BiG3 and BiG5), as obtained at three different frequencies. For all the samples, ε_r first increases slowly with temperature and then above 1070 K it starts to grow abruptly, reaching a maximum at a temperature close to 1100 K. The dielectric anomaly (peak in ε_r vs. T curve) is frequency independent and the temperature of the permittivity maximum matches well with

14

that of the endothermic DSC peak for each composition (see Fig. 1b). In our earlier work we have demonstrated that the dielectric permittivity peak of similar four-layered $Bi_{4.25}La_{0.75}Ti_3Fe_{0.5}Co_{0.5}O_{15}$ Aurivillius ceramics at about 1100 K corresponds to the ferroelectric Curie temperature, T_c^{FE}.[22] Lomanova $et\ al.$ have reported on second-order-type ferroelectric phase transitions occurring between 900 K and 1100 K in multi-layered Aurivillius compounds.[35] Here, the ferroelectric Curie temperature T_c^{FE} decreases from 1103 K (BiG1) to 1098 K (BiG3) as the amount of the Co added is increased from x=0 to x=0.5. Both these temperatures are higher than that of pure BFTO (~1023 K [30]), but they are close to the ferroelectric Curie temperature of BLFCT ceramics (T_c^{FE} ~1060 K [22]) where we used more polarizable lanthanum atoms as the A-site substituent instead of gadolinium. The additional partial replacement of Ti^{4+} ions by Nb^{5+} ions shifts the T_c^{FE} to lower temperatures, leading to the ferroelectric transition of BiG5 at about 1095 K.
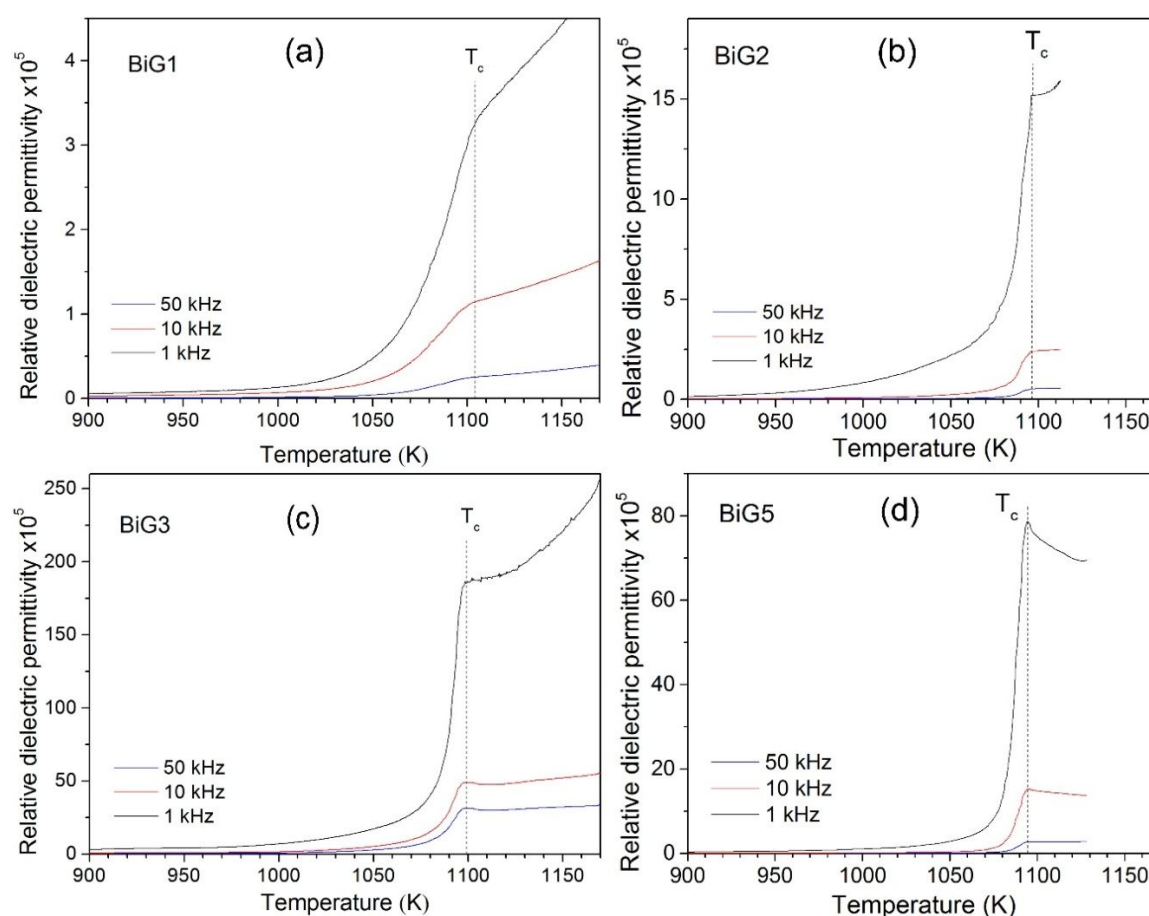

Fig. S10. Temperature dependence of the relative dielectric permittivity of (a) BiG1, (b) BiG2, (c) BiG3, and (d) BiG5 samples, as obtained at three different frequencies (1 kHz, 10 kHz and 50 kHz).

Below T_c^{FE}, the dielectric response of BFTO-derived Aurivillius multiferroics with $3d$ transition metal ions at B sites is often perturbed by extrinsic effects such as interfacial polarization [73] and two-site polaron hoping mechanism [21] originating from charge defects (e.g., oxygen vacancies, valence fluctuation of Fe/Co ions). As a consequence (of a change in conductive mechanism), a bump shoulder in the ε_r-T plot has been typically observed at temperatures around 600 K, and this broad peak was found to decrease and shift toward a higher temperature when the testing frequency is increased.[28]
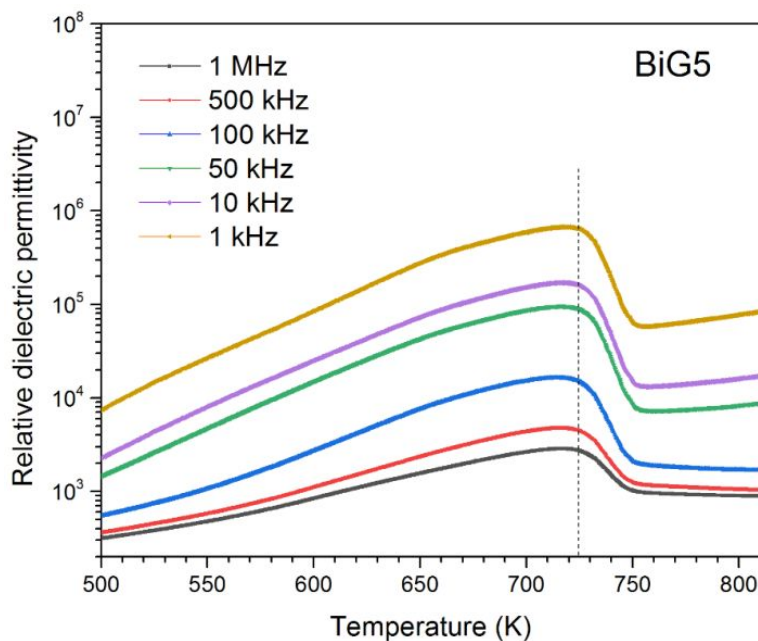

Figure S11.   Temperature dependence of the relative dielectric permittivity of the BiG5 sample, as recorded in the temperature interval 500-800 K.

To investigate the dielectric response of our samples for a possible relaxation from extrinsic effects at lower temperatures, the relative dielectric permittivity and loss tangent of the samples were investigated in the temperature range 500-800 K at 1 kHz, 10 kHz, 50 kHz, 100 kHz, 500 kHz and 1 MHz. The representative plot for the BiG5 sample is shown in Fig. S11. From the figure, one can see that there is a peak in the temperature dependence of ε_r, but its maximum at about 725 K is independent on the frequency. This temperature is much higher than that of the ferrimagnetic-to-paramagnetic temperature of the spinel oxide $FeCo_2O_4$ (~460 K [49]) and lower than T_c of single phase $CoFe_2O_4$ (~785-860 K [74]), but close to the Curie temperature of the nonstoichiometric $Co_{1.2}Fe_{1.8}O_4$ [$Co^{2+}_{0.5}Fe^{3+}_{0.5}(Co^{2+}_{0.5}Co^{3+}_{0.2}Fe^{3+}_{1.3})O_4$] spinel ($T_{cm}$=714 K [74]), which is known of the presence of valence fluctuations of the magnetic

16

atoms. It should be noted that the magnetic moment of this kind of spinel is the smallest ($\sim 2.7 \mu_B$) of all ferrites in the $Co_xFe_{3-x}O_4$ and $Co_{2-x}Ti_{1-x}Fe_{2x}O_4$ series [74,75], and thus a small amount (below the detection limit of the X-ray diffractometer) of this magnetic impurity, if present, hardly can contribute significantly to the measured magnetization at room temperature ($M_s \sim 3.5$ emu/g). On the other hand, the mixed valence state of magnetic cations in the spinel oxide, as mentioned above, could be partially responsible for leaky polarization *vs.* electric field (P-E) hysteresis loops.
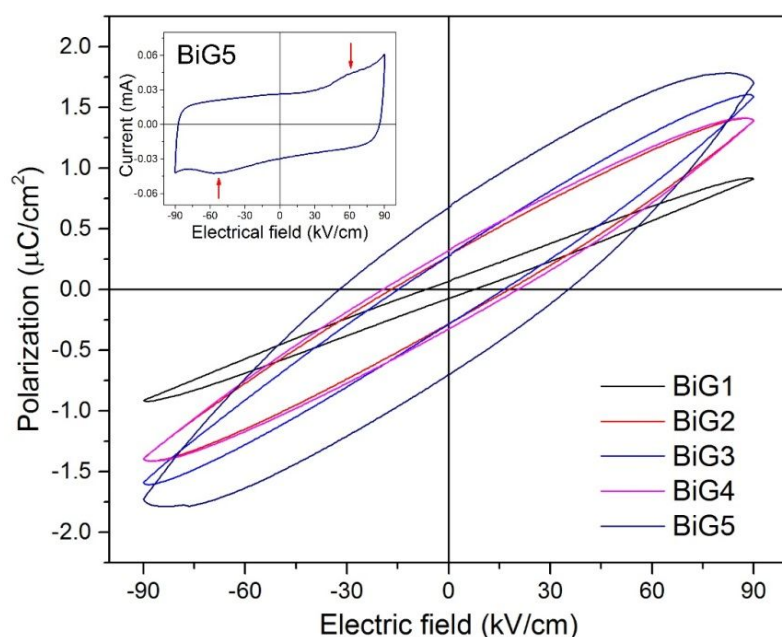

Figure S12. Polarization *vs*. electric field curves of the BiG1-BiG5 samples (at 10 Hz). The red arrows in the inset point to broad peaks on the field-dependent electrical current, indicating ferroelectric switching in BiG5.

Fig. S12 displays the P-E curves of all the samples, as recorded at room temperature and a frequency of the applied electric field of 100 Hz. Apparently, due to a large DC conductivity, the loops are not saturated even under a high driving electric field of 90 kV/cm. The presence of structural defects and low density ($\sim$89-92% of the theoretical density) caused the dielectric break-down of the samples when the field above 90 kV/cm was applied in ferroelectric tests. It should be mentioned that such low-quality "banana-type" P-E loops are quite usual for multiferroic BFTO-derived systems, where conductive Fe ions together with oxygen vacancies contribute to the increased electrical conduction.[19,76] The ferroelectricity in the Aurivillius materials was evidenced by observation of weak current peaks on the I-E curves (see the inset of Fig. S12).

17

References

[65] S. Chatterjee, S. Giri, S. K. De, S. Majumdar, Reentrant-spin-glass state in Ni2Mn1.36Sn0.64 shape-memory alloy, *Physical Review B*, 2009, **79**, 092410.

[66] M. Viswanathan, P. S. A. Kumar, Observation of reentrant spin glass behavior in LaCo0.5Ni0.5O3, *Physical Review B*, 2009, **80**, 012410.

[67] K. Vijayanandhini, C. Simon, V. Pralong, V. Caignaert, B. Raveau, Spin glass to cluster glass transition in geometrically frustrated CaBaFe4−xLixO7 ferrimagnets, *Physical Review B*, 2009, **79**, 224407.

[68] P. C. Hohenberg, B. I. Halperin, Theory of dynamic critical phenomena, *Reviews of Modern Physics*, 1977, 49, 435-479.

[69] J. Dho, W. S. Kim, N. H. Hur, Reentrant Spin Glass Behavior in Cr-Doped Perovskite Manganite, *Physical Review Letters*, 2002, **89**, 027202.

[70] I. Skorvanek, S. Skwirblies, J. Kotzler, Magnetic hardening and spin-glass phenomena in nanocrystalline FeNbB at low temperatures, *Physical Review B*, 2001, **64**, 184437.

[71] J. L. Tholence, R. Tourner, Susceptibility and remanent magnetization of a spin glass, *Journal de Physique Colloques*, 1974, **35**, C4-229-235.

[72] S. Garcia, L. Ghivelder, S. Soriano, I. Felner, Magnetization scaling in the ruthenate-cuprate RuSr2Eu1.4Ce 0.6Cu2O10-δ (Ru-1222), *European Physical Journal B*, 2006, **53**, 307-313.

[73] M. S. Wu, Z. M. Tian, S. L. Yuan, H. N. Duan, Y. Qiu, Dielectric behavior and ac conductivity in Aurivillius Bi4Ti3O12 doped by antiferromagnetic BiFeO3, *Physics Letters A*, 2012, **376**, 2062-2066.

[74] Q. C. Sun, C. S. Birkel, J. Cao, W. Tremel, J. L. Musfeldt, Spectroscopic Signature of the Superparamagnetic Transition and Surface Spin Disorder in CoFe2O4Nanoparticles, *ACS Nano*, 2012, **6**, 4876-4883.

[75] P. Nathwani, V. S. Darshane, Structural, transport, magnetic and infrared studies of the oxidic spinels Co2-xTi1-xFe2xO4, *Journal of Physics C: Solid State Physics*, 2000, **21**, 3191-3203.

[76] S. Liu, S. Yan, H. Luo, L. Yao, Z. Hu, S. Huang, L. Deng, Enhanced magnetoelectric coupling in La-modified Bi5Co0.5Fe0.5Ti3O15 multiferroic ceramics, *Journal of Materials Science*, 2018, **53**, 1014-1023.

18